

AN INNER WIRE CHAMBER FOR THE
MEASUREMENT OF $K^+ \rightarrow \pi^+ \nu \bar{\nu}$

by

Vincent A. Kujala

B.Sc., University of Victoria, 1989

A Thesis Submitted in Partial Fulfillment
of the Requirements for the Degree of

ACCEPTED

SCHOOL OF GRADUATE STUDIES

MASTER OF SCIENCE

in the Department of
Physics and Astronomy

DEAN

92/02/27

We accept this thesis as conforming
to the required standard

Dr. D. Bryman, Co-Supervisor, (Department of Physics & Astronomy)

Dr. L. Robertson, Co-Supervisor, (Department of Physics & Astronomy)

Dr. G. Mason, Departmental Member, (Department of Physics & Astronomy)

Dr. H. Kwok, Outside Member, (Department of Electrical Engineering)

Dr. M. Hasinoff, External Examiner, (Department of Physics, UBC)

© VINCENT A. KUJALA, 1991
University of Victoria

*All rights reserved. This thesis may not be reproduced
in whole or in part by mimeograph or other means,
without the permission of the author.*

Supervisor: Dr. Douglas Bryman

ABSTRACT

A thin cylindrical drift chamber with helical cathode strips for measuring the z coordinate of charged particle tracks is described. The motivations for adding the chamber to the existing detector of Brookhaven experiment E787 are discussed. The results of a Monte Carlo study of the momentum resolution of the detector with the chamber are presented. The methods of construction and calibration are detailed. Results from a positioning and position resolution study using cosmic ray data are presented. Results from a momentum resolution study using the mono-energetic kaon decays, $K^+ \rightarrow \pi^+ \pi^0$ and $K^+ \rightarrow \mu^+ \nu_\mu$, are presented and compared with Monte Carlo results.

Examiners:

[Redacted]

Dr. D. Bryman, Co-Supervisor, (Department of Physics & Astronomy)

[Redacted]

Dr. L. Robertson, Co-Supervisor, (Department of Physics & Astronomy)

[Redacted]

Dr. G. Mason, Departmental Member, (Department of Physics & Astronomy)

[Redacted]

Dr. H. Kwok, Outside Member, (Department of Electrical Engineering)

[Redacted]

Dr. M. Hasinoff, External Examiner, (Department of Physics, UBC)

Table of Contents

Title	i
Abstract	ii
Table of Contents	iii
List of Tables	v
List of Figures	vi
Acknowledgements	viii
1 Introduction	1
1.1 E787 Physics	1
1.2 E787 Detector	1
1.3 E787 Drift Chamber	4
1.4 Motivation for the Inner Wire Chamber	4
1.5 Momentum Resolution Factors	5
2 Monte Carlo Study of IWC	9
2.1 Description of Software	9
2.2 Results From Monte Carlo Study	10
3 IWC Geometry and Construction	18
3.1 Geometry	18
3.2 Description of Operation	22
3.3 Construction	23
4 Electronics	32
4.1 Preamplifier Schematics and Description	32
4.2 Postamplifier Description	33
5 Chamber Tests	34

6	Calibration	38
6.1	Time to Digital Converters	38
6.2	Analog to Digital Converters	38
6.3	Calibration Verification	40
7	Cosmic Ray Study	47
7.1	Description	47
7.2	Space Time Relation	48
7.3	Rotation	49
7.4	Translation	51
7.5	Results	53
8	Momentum Resolution Study	56
8.1	Description	56
8.2	Comparison with Monte Carlo Results	57
9	Conclusions	62
	Bibliography	63
	Suggested Reading	65
	Glossary	66

List of Tables

1	X Geometry used for estimating multiple scattering.	11
2	Cumulative RMS of Lateral Displacement (mm) for pions.	12
3	Energy and Momentum loss for pions.	12
4	ΔP_{xy} and ΔP_z with and without the IWC.	14
5	Individual xy and z contributions from IWC.	14
6	Momentum resolution versus position resolutions in IWC.	15
7	Measured wire densities.	27
8	IWC wire tensions from tension meter, February 23/24, 1991.	28
9	Fe ⁵⁵ pulse heights vs HV. Ar/Et 50/50, 100cc/min.	35
10	IWC current vs high voltage	35
11	IWC orientation results from cosmic study.	54
12	Isochrones and Drift Laws with B = 0 kG and IWC voltage = 2.0 kV	26
12	Momentum resolution results.	57
14	Drift velocity for Argon/Dihane 50/50 gas (from GARFIELD)	24
16	Copper strips on inner foil	26
16	Measured wire tensions	29
17	Close up view of up stream end of IWC	30
18	Close up view of down stream end of IWC	31
19	IWC preamplifier schematic	33
20	Fe ⁵⁵ pulse height vs voltage	36
21	Typical Fe ⁵⁵ pulse height on anode wire.	36
22	Typical Fe ⁵⁵ pulse height on cathode strip.	37
23	Scopin anode wire TDC spectrum.	39

List of Figures

24	Sample cathode strip TDC spectrum	39
25	Example anode wire ADC spectrum	41
26	Sum of anode wire ADC spectra	41
27	Example cathode strip ADC spectrum	42
28	Cathode - anode TDC times for each anode	42
29	Cathode - anode TDC times for each cathode	44
30	Improvement in c-a means for wires	44
1	XY cross section of E787 detector.	2
2	RZ cross section of E787 detector.	2
3	Magnetic field for E787 detector.	7
4	DC minus UMC xy momentum.	11
5	DC minus UMC z momentum.	13
6	DC minus UMC / UMC total momentum resolution.	13
7	Momentum resolution versus IWC xy resolution.	16
8	Momentum resolution versus IWC z resolution.	16
9	Final UMC $K\pi 2$ momentum for DC alone.	17
10	Final UMC $K\pi 2$ momentum for DC and IWC.	17
11	XY cross section of IWC	19
12	Isochrones and Drift Lines with $B = 0$ kG and IWC voltage = 2.0 kV	20
13	Isochrones and Drift Lines with $B = 10$ kG and IWC voltage = 2.0 kV	21
14	Drift velocity for Argon/Ethane 50/50 gas (from GARFIELD)	24
15	Copper strips on inner foil	26
16	Measured wire tensions	29
17	Close up view of up stream end of IWC	30
18	Close up view of down stream end of IWC	31
19	IWC preamplifier schematic.	33
20	Fe^{55} pulse height vs voltage	36
21	Typical Fe^{55} pulse height on anode wire.	36
22	Typical Fe^{55} pulse height on cathode strip.	37
23	Sample anode wire TDC spectrum.	39

24	Sample cathode strip TDC spectrum.	39
25	Example anode wire ADC spectrum.	41
26	Sum of anode wire ADC spectra.	41
27	Example cathode strip ADC spectrum.	42
28	Sum of cathode strip ADC spectra.	42
29	Cathode - anode TDC times for each anode.	43
30	Cathode - anode TDC times for each cathode.	44
31	Improvement in c-a means for wires.	44
32	Improvement in c-a means for strips.	45
33	Improvement in c-a sigmas for wires.	45
34	Improvement in c-a sigmas for strips.	46
35	Strip ADC sum vs anode ADC.	46
36	IWC efficiency versus high voltage for $K\mu 2$ data.	48
37	Anode TDC vs POCA.	49
38	Fit of TDC vs POCA (a) and its derivative (b).	50
39	IWC-DC phi before positioning.	51
40	IWC-DC z before positioning.	52
41	Number of strips per cluster per wire.	52
42	Number of valid anode wires near expected hit.	53
43	IWC-DC phi after positioning.	54
44	IWC-DC z after positioning.	55
45	Energy-Range plot for $K\pi 2$ sample.	57
46	Energy-Range plot for $K\mu 2$ sample.	58
47	$K\pi 2$ final momentum spectrum without IWC.	58
48	$K\pi 2$ final momentum spectrum with IWC.	59
49	$K\mu 2$ final momentum spectrum without IWC.	59
50	$K\mu 2$ final momentum spectrum with IWC.	60

Acknowledgments

I would like to thank my supervisor, Doug Bryman of the Department of Physics and Astronomy, for his encouragement, patience, and advice during my involvement with E787. I would also like to thank Yoshi Kuno for the work he did for the Monte Carlo study and for the diagrams of the E787 detector, and also to recognize Paul Padley for the work he performed during the development of the IWC software. In addition, I would like to acknowledge John Creswell for designing the IWC pre-amplifiers and to thank Chapman Lim for constructing the IWC. Finally, I would like to thank Doug, Yoshi, Paul, Toshio Numao, and Akira Konaka for reading and correcting earlier versions of this thesis.

1.2 E787 Detector

The E787 detector, located at BNL's Alternating Gradient Synchrotron facility, is briefly described below. Figures 1 and 2 illustrate xy and rz cross section views of the E787 detector[5].

A threshold Cherenkov counter is used to identify kaons with a momentum of 800 MeV/c and to reject pions from the AOS kaon production target and also pions which result from kaon

Chapter 1

Introduction

1.1 E787 Physics

Experiment E787 at Brookhaven National Laboratory is an experiment designed to look for the second order weak decay, $K^+ \rightarrow \pi^+ \nu \bar{\nu}$. The branching ratio for this decay is sensitive to the top quark mass and the Cabbibo-Kobiashi-Maskawa (CKM) matrix elements: V_{ts} , V_{cs} , V_{td} , V_{cd} , and V_{us} [1,2,3]. The expected branching ratio is in the range $(1 \leftrightarrow 4) * 10^{-10}$ for a top quark mass in the range $150 \pm 25 \text{ GeV}/c^2$ [4]. The range of the expected branching ratio is due to the uncertainties in the CKM matrix elements. A measurement of the branching ratio would further constrain the matrix elements and a measurement of $K^+ \rightarrow \pi^+ \nu \bar{\nu}$ outside the expected range would suggest new physics and a need for theory beyond the standard model[5]. E787's last official branching ratio limit is $\text{BR}(K^+ \rightarrow \pi^+ \nu \bar{\nu}) < 3.4 * 10^{-8}$ from 1988 data, and a preliminary result for 1989 data is $\text{BR}(K^+ \rightarrow \pi^+ \nu \bar{\nu}) < 5 * 10^{-9}$.

1.2 E787 Detector

The E787 detector, located at BNL's Alternating Gradient Synchrotron facility, is briefly described below. Figures 1 and 2 illustrate xy and rz cross section views of the E787 detector[6].

A threshold Cherenkov counter is used to identify kaons with a momentum of $800 \text{ MeV}/c$ and to reject pions from the AGS kaon production target and also pions which result from kaon

in-flight decays. These pions may scatter into the detector and create a false $K^0 \rightarrow \pi^+\pi^0$ signal.

A BeO degrader of length, 500 cm, is located upstream of the target. The beam then enters a 10 cm diameter target made of BeO. The beam travels along the beam axis. The visible energy released by the beam is stopped and the products are detected. The products are then stopped and the smaller visible energy is detected. The products are then stopped and the smaller visible energy is detected.

The kaon decay products (pions, muons, electrons) are tracked in a cylindrical drift chamber with 2x steradian angular coverage. The drift chamber is centered on the target. The active volume of the drift chamber extends from 45.1 cm to 89.5 cm. A one tesla magnetic field enables a momentum measurement of the charged decay products.

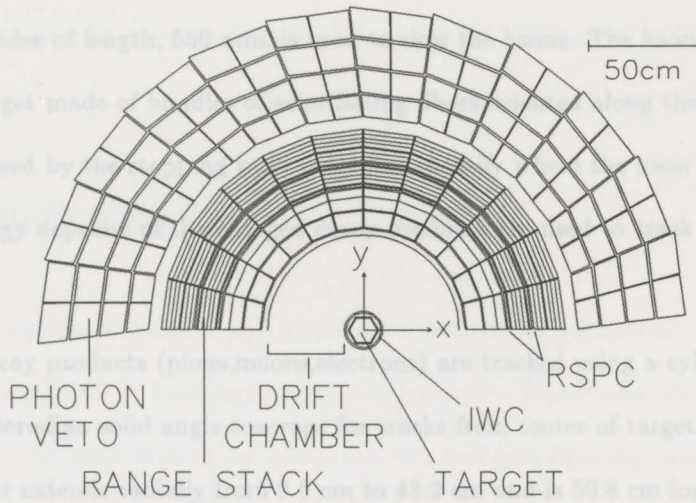


Figure 1: XY cross section of E787 detector.

The range and energy of the charged decay products are then measured in a plastic scintillator range stack which is segmented into 24 azimuthal sectors and 15 radial layers from 45.1 cm to 89.5 cm. The light is read from both ends of the 1.3 meter segments with photomultiplier tubes and the signal is sent to 500 MHz treatment systems which are used to look for the $\pi^0 \rightarrow \mu^+\mu^-$ decay chain ($\pi^0 \rightarrow \mu^+\mu^- \rightarrow \pi^+\pi^-\nu_\mu\nu_\mu$) for unambiguous pion identification. Also included in the range stack are 15 layers of RSPC (Radially Segmented Proportional Counter) using serpentine cathodes.

Suppression of background is achieved by a photon veto system covering the full 4π solid angle. The photon veto system is composed of 15 layers of scintillator (5 mm) layers. The barrel section is segmented into 24 azimuthal sectors covering radial thickness of 45.3 cm and axial length of 1.3 m. The end cap sections are segmented into 24 azimuthal sectors with the lead-scintillator stacks in the axial direction.

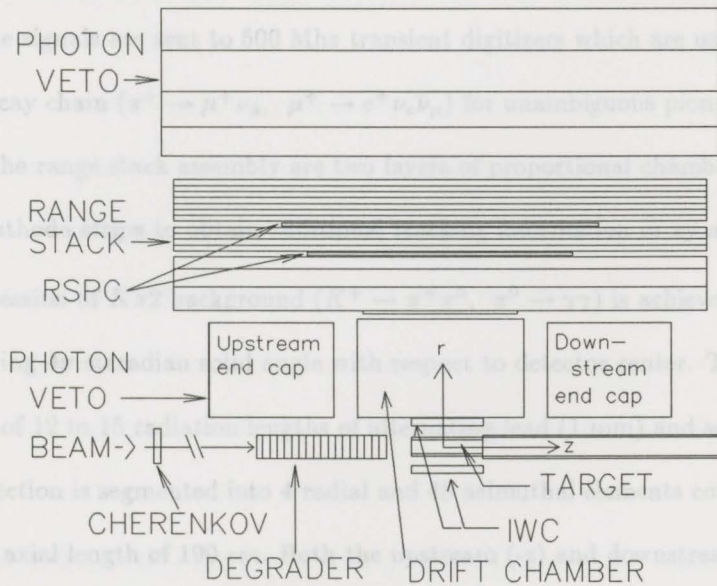


Figure 2: RZ cross section of E787 detector.

The one tesla field is provided by a conventional water-cooled solenoidal magnet which encompasses the detector within its inner volume, 2.22 m long by 2.96 m diameter.

in-flight decays. These pions may scatter into the detector and create a false $K^+ \rightarrow \pi^+ \nu \bar{\nu}$ signal.

A BeO degrader of length, 550 mm, is used to slow the kaons. The kaons come to rest in a 10 cm diameter target made of bundles of scintillating fibers oriented along the beam axis. The visible energy released by the stopping kaon is used to identify where the kaon stopped and the smaller visible energy deposits of the charged decay products are used to track the products out of the target.

The kaon decay products (pions, muons, electrons) are tracked using a cylindrical drift chamber with 2π steradian solid angle coverage for tracks from center of target. The active volume of the drift chamber extends radially from 9.5 cm to 43.2 cm and is 50.8 cm long. A one tesla magnetic field enables a momentum measurement of the charged decay products.

The range and energy of the charged decay products are then measured in a plastic scintillator range stack which is segmented into 24 azimuthal sectors and 15 radial layers from 45.1 cm to 89.6 cm. The light is read from both ends of the 1.8 meter segments with photomultiplier tubes and the signals are sent to 500 Mhz transient digitizers which are used to look for the $\pi - \mu - e$ decay chain ($\pi^+ \rightarrow \mu^+ \nu_\mu$, $\mu^+ \rightarrow e^+ \nu_e \bar{\nu}_\mu$) for unambiguous pion identification. Also included in the range stack assembly are two layers of proportional chambers (RSPC) using serpentine cathode strips to obtain additional tracking information in xy and z coordinates.

Suppression of $K\pi 2$ background ($K^+ \rightarrow \pi^+ \pi^0$, $\pi^0 \rightarrow \gamma\gamma$) is achieved with a photon veto system covering 4π steradian solid angle with respect to detector center. The photon veto system is composed of 12 to 15 radiation lengths of alternating lead (1 mm) and scintillator (5 mm) layers. The barrel section is segmented into 4 radial and 48 azimuthal elements covering radial thickness of 45.3 cm and axial length of 190 cm. Both the upstream (-z) and downstream (+z) end cap sections are segmented into 24 azimuthal sectors with the lead-scintillator stacks in the axial direction.

The one tesla field is provided by a conventional water-cooled solenoidal magnet which encompasses the detector within its inner volume, 2.22 m long by 2.96 m diameter.

1.5 For pions from $K\pi^2$ decay (using 1988 data), the detector has a momentum resolution of 2.5%, a combined target and range-stack energy resolution of 3.0%, and a range-stack range resolution of 3% [7].

1.3 E787 Drift Chamber

The drift chamber consists of 5 radial layers with each layer being azimuthally segmented into 36,40,50,60,70 cells respectively from inner layer to outer layer. Layers one, three, and five have six instrumented wires with axial orientation and layers two and four have six wires with stereo angles from 3.1 to 4.0 degrees with respect to the z-axis of the chamber. The innermost instrumented wire is at radius 12.7 cm and the outer most wire at radius 37.6 cm. The gas used is an argon,ethane,ethanol mixture (49.9/49.9/0.2) at atmospheric pressure [9].

1.4 Motivation for the Inner Wire Chamber

The primary motive for constructing the Inner Wire Chamber (IWC) is to improve the momentum resolution of the detector by adding an extra measurement of the track between the target and the drift chamber. This results in better particle identification when used in conjunction with range and energy measurements from other elements of the detector.

A secondary motive for the IWC is to improve the z-tracking and consequently the dip-angle measurement and energy loss corrections in the target and range stack; dip-angle is defined as angle of track from the z-axis of the detector.

The third motive is to prototype a future E787 drift chamber called the UTC (Ultra Thin Chamber) [10,11,12]. The UTC is an attempt to reduce the multiple scattering contribution to momentum resolution by using three spaced layers (for long arc-length) and helium gas between these layers. The IWC z-measurement technique (Chapter 3) will be used in the UTC.

1.5 Momentum Resolution Factors

There are three basic factors affecting the momentum resolution of the drift chamber: position measurement error, multiple scattering in the gas, and magnetic field nonuniformity.

The curvature error is the square-root of the sum of squares of measurement error and multiple scattering error [13]:

$$(\delta k)^2 = (\delta k_{res})^2 + (\delta k_{ms})^2 \quad (1)$$

The following relation is used to obtain an estimate of the measurement error from the xy-position measuring error of the wires. The equation assumes equally spaced wires, but for this case the wires are not equally spaced hence it is used here as an approximation:

$$\delta k_{res} \approx \frac{\epsilon}{L^2} \left(\frac{720}{N+5} \right)^{1/2}$$

where :

ϵ = xy position measurement error

L = arc length of track

N = number of position measurements

(2)

With $\epsilon = 150\mu\text{m}$, $L \approx 25\text{cm}$, and $N = 18$ (from the axial layers) the curvature error due to the wire position measurement error is estimated as, $\delta k_{res} \approx 1.34 * 10^{-4}\text{cm}^{-1}$.

The following equation is used to obtain the curvature error due to multiple scattering in the gas of the drift chamber:

$$\delta k_{ms} \approx \frac{16 \text{ MeV}/c}{L p \beta \cos^2 \lambda} \left(\frac{L}{X_0} \right)^{1/2}$$

where :

L = arc length of track

p = particle momentum (MeV/c)

β = velocity relative to speed of light

λ = angle from xy plane

X_0 = radiation length of scattering medium

(3)

With $L = 25\text{cm}$, $p = 205\text{MeV}/c$, $\beta = 0.826$ (for pion from kaon decay), $\cos \lambda \approx 1.0$, and $X_0 = 1.18 * 10^4\text{cm}$ the curvature error due to multiple scattering is estimated as,
 $\delta k_{ms} \approx 1.74 * 10^{-4}\text{cm}^{-1}$.

The total curvature error is estimated as, $\delta k \approx 2.2 * 10^{-4}\text{cm}^{-1}$. For pions of momentum, 205 MeV/c, this curvature error corresponds to a radius of curvature ($R = 1/k$) error of 1.5% (radius equals 68 cm).

The following equation is used to obtain the momentum from the measured radius of curvature:

$$p \cos \lambda = 0.3 \left(\frac{\text{MeV}/c}{\text{kG} \cdot \text{cm}} \right) z B R$$

where :

p = particle momentum (MeV/c)

λ = angle from xy plane

z = charge in units of e ($1.6 \cdot 10^{-19}$ coulomb)

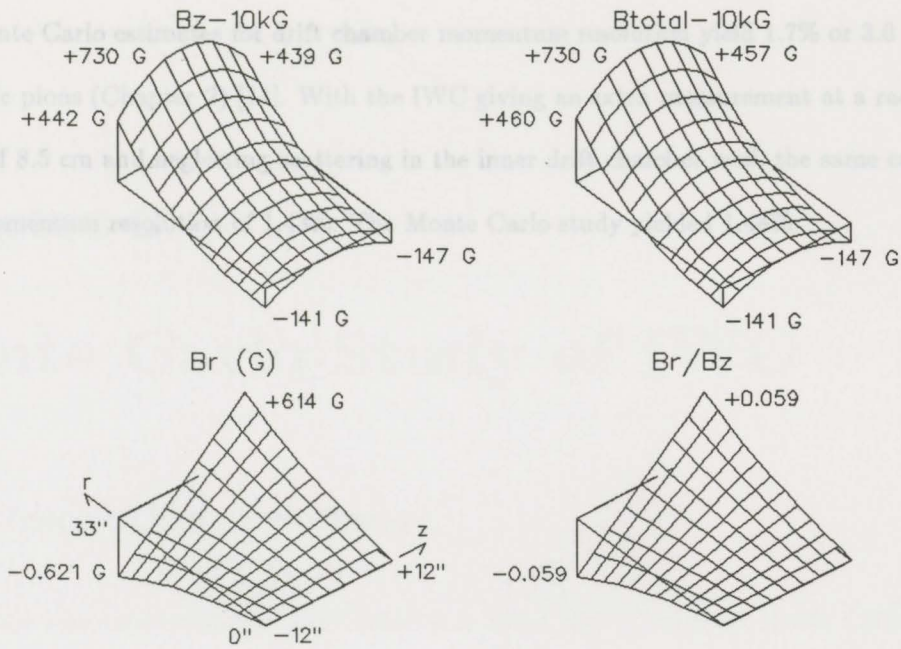


Figure 3: Magnetic field for E787 detector.

B = magnitude of magnetic field (kG)

R = radius of curvature (cm)

(4)

The equation above suggests that the error in the magnetic field and the error in the radius of curvature should be added in quadrature to obtain the total momentum error. The geometry of the detector restricts the selection of tracks to $-\pi/6 < \lambda < +\pi/6$, consequently the error of λ is ignored.

The magnetic field was measured before insertion of detector (in 1988) and the nonuniformity was found to be 0.6% over the region of the drift chamber. This error added in quadrature with above estimated error for radius yields an estimated momentum resolution of 1.6%. Figure 3 is an illustration of the measured magnetic field.

Monte Carlo estimates for drift chamber momentum resolution yield 1.7% or 3.0 MeV/c for 205 MeV/c pions (Chapter 2) [14]. With the IWC giving an extra measurement at a radial distance of 8.5 cm and neglecting scattering in the inner drift chamber wall, the same calculations yield a momentum resolution of 1.43%. The Monte Carlo study yielded 1.44%.

Monte Carlo Study of IWC

2.1 Description of Software

The software used to simulate the E787 detector is called UMC (Universal Monte Carlo). This code is based on the EGS (Electron Gamma Shower) software [16]. The Monte Carlo code produces data that can be analyzed with the standard analysis code of E787 called KOFIA (Korn Offline Interactive Analysis).

The UMC code was modified to write the energies, positions, and directions of each track just before entering the drift chamber. The information was written in a special data bank which was later read by modified KOFIA code and used to project the track back to the IWC radius. The expected intersection position was then smeared with realistic position resolutions and added to xy and x - ψ fits.

The DC tracking code (in KOFIA) first performs a circle fit of axial wire data in the xy plane, then uses this track to calculate z position and angle of rotation (turning angle, ψ) with respect to the point on xy -circle closest to $(x=0, y=0)$. The z position is obtained by assuming stereo wires are axial, thus calculating a false xy position, then correcting this false position via x and y translations that are parameterized by z , and demanding that the new x and y positions lie on the previously found xy -circle. The new z and y coordinates are then used to calculate the turning angle, ψ . The displacement of the false position is assumed to be due to the stereo angle

of the wires. This method is sensitive to the xy-tracking resolution and the positioning of the stereo wires.

The IWC was not simulated within the UMC code since the multiple scattering within the drift chamber, the inner drift chamber wall was simulated within the Monte Carlo. In addition, it was computationally advantageous to simulate the IWC position resolution within the UMC code. The DC code was similarly projected, smeared, and added to the DC code. Table 2 estimates energy and momentum losses due to the IWC and DC [16].

Chapter 2

Monte Carlo Study of IWC

2.1 Description of Software

The software used to simulate the E787 detector is called UMC (Universal Monte Carlo). This code is based on the EGS (Electron Gamma Shower) software [15]. The Monte Carlo code produces data that can be analyzed with the standard analysis code of E787 called KOFIA (Kaon Offline Interactive Analysis).

The UMC code was modified to write the energies, positions, and directions of each track just before entering the drift chamber. The information was written in a special data bank which was later read by modified KOFIA code and used to project the track back to the IWC radius.

The expected intersection position was then smeared with realistic position resolutions and added to xy and z-psi fits.

The DC tracking code (in KOFIA) first performs a circle fit of axial wire data in the xy plane, then uses this track to calculate z position and angle of rotation (turning angle, psi) with respect to the point on xy-circle closest to $(x=0, y=0)$. The z position is obtained by assuming stereo wires are axial, thus calculating a false xy position, then correcting this false position via x and y translations that are parameterized by z, and demanding that the new x and y positions lie on the previously found xy-circle. The new x and y coordinates are then used to calculate the turning angle, psi. The displacement of the false position is assumed to be due to the stereo angle

of the wires. This method is sensitive to the xy-tracking resolution and the positioning of the stereo wires.

The IWC was not simulated within the UMC code since the multiple scattering within the IWC is negligible; however, the inner drift chamber wall was simulated within the Monte Carlo. In addition, it was computationally advantageous to simulate the IWC position resolution within the KOFIA code rather than the time consuming UMC code. Table 2 estimates multiple scattering effects of the IWC and DC, and Table 3 estimates energy and momentum losses due to the IWC and DC [16].

The information in the data bank written by UMC was used to project the xy-track to the radius of the IWC anode wires to determine which anode wire was hit. Then, the track's point of closest approach to that wire was calculated and smeared with a Gaussian distribution in both the x and y coordinates. The resulting xy position was added as the last sample point in the DC xy track fit. The z-psi track from the DC code was similarly projected, smeared, and added to the DC z-psi track fit.

2.2 Results From Monte Carlo Study

The transverse (xy) and longitudinal (z) momentum resolutions were obtained by looking at the difference between the DC measured and UMC expected momenta, then fitting a Gaussian to the resulting momentum spectrum. The standard deviation parameter of the fit was defined as the momentum resolution. Figure 4 shows xy momentum difference, figure 5 shows z momentum difference, figure 6 shows the relative momentum resolution obtained from ratio of total momentum difference over UMC expected momentum. These momentum resolutions are the intrinsic drift chamber momentum resolutions. They are independent of such factors as energy loss and scattering within the target.

The intrinsic xy-momentum resolution was observed to improve by 15% while the intrinsic

Table 1: Geometry used for estimating multiple scattering.

Media	Description	Thickness (cm)	Rad. Length (g/cm ²)	Density (g/cm ³)
CU	Inner Ground Plane	0.00254	12.864	8.96
G10	Inner Support	0.0381	29.081	1.70
WCH-GAS	Inner Dead Space	0.35	23.024	0.00195
KAPTON	Inner Foil	0.00508	40.556	1.43
CU	Inner Strips	0.00001	12.864	8.96
WCH-GAS	Inner Active Reg	0.55	23.024	0.00195
WCH-GAS	Outer Active Reg	0.55	23.024	0.00195
CU	Outer Strips	0.00001	12.864	8.96
KAPTON	Outer Foil	0.00508	40.556	1.43
WCH-GAS	Outer Dead Space	0.35	23.024	0.00195
KAPTON	Outer Ground Foil	0.00508	40.556	1.43
CU	Outer Ground Plane	0.00001	12.864	8.96
AIR	IWC-DC Gap	0.01	37.008	0.00129
G10	Inner Support	0.06096	29.081	1.312
MYLAR	Inner Foil	0.00508	39.920	1.390
CU	Inner Ground Plane	0.00001	12.864	8.96
WCH-GAS	Active Region	33.7	23.024	0.00195
CU	Outer Ground Plane	0.00001	12.864	8.96
MYLAR	Outer Foil	0.00508	39.920	1.390
G10	Outer Support	0.0716	29.081	1.31

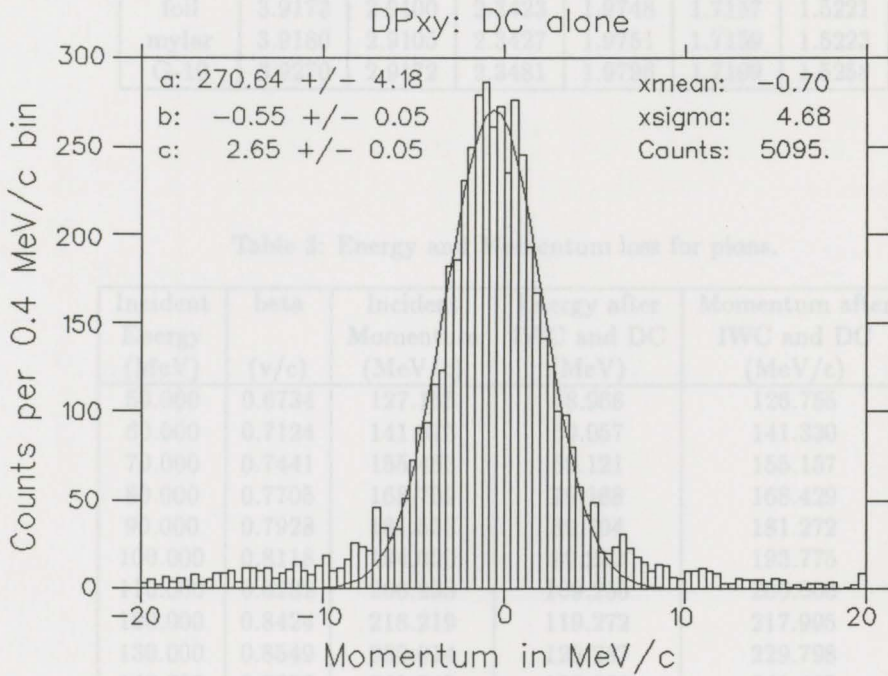


Figure 4: DC minus UMC xy momentum.

Table 2: Cumulative RMS of Lateral Displacement (mm) for pions.

Kinetic Energy	50.0 (MeV)	70.0 (MeV)	90.0 (MeV)	110.0 (MeV)	130.0 (MeV)	150.0 (MeV)
-IWC-	—	—	—	—	—	—
Cu	0.0001	0.0001	0.0000	0.0000	0.0000	0.0000
G-10	0.0024	0.0018	0.0014	0.0012	0.0010	0.0009
gap	0.0292	0.0217	0.0175	0.0148	0.0128	0.0114
Kapton strips	0.0296	0.0220	0.0177	0.0149	0.0130	0.0115
i-act wires	0.0725	0.0540	0.0435	0.0367	0.0319	0.0283
o-act strips	0.1156	0.0860	0.0693	0.0584	0.0508	0.0451
Kapton gap	0.1160	0.0863	0.0695	0.0586	0.0510	0.0452
film	0.1440	0.1071	0.0863	0.0728	0.0632	0.0561
foil	0.1444	0.1074	0.0865	0.0730	0.0634	0.0563
air	0.1452	0.1080	0.0870	0.0734	0.0638	0.0566
-DC-	—	—	—	—	—	—
G-10	0.1502	0.1117	0.0900	0.0759	0.0659	0.0585
mylar	0.1507	0.1121	0.0903	0.0762	0.0662	0.0587
foil	0.1507	0.1121	0.0903	0.0762	0.0662	0.0587
active foil	3.9173	2.9100	2.3423	1.9748	1.7157	1.5221
mylar	3.9173	2.9100	2.3423	1.9748	1.7157	1.5221
G-10	3.9180	2.9105	2.3427	1.9751	1.7159	1.5223
	3.9270	2.9172	2.3481	1.9796	1.7199	1.5258

Table 3: Energy and Momentum loss for pions.

Incident Energy (MeV)	beta (v/c)	Incident Momentum (MeV/c)	Energy after IWC and DC (MeV)	Momentum after IWC and DC (MeV/c)
50.000	0.6734	127.155	48.966	126.755
60.000	0.7124	141.673	59.057	141.330
70.000	0.7441	155.463	69.121	155.157
80.000	0.7705	168.709	79.168	168.429
90.000	0.7928	181.533	89.204	181.272
100.000	0.8118	194.020	99.232	193.775
110.000	0.8282	206.233	109.255	206.000
120.000	0.8424	218.219	119.272	217.995
130.000	0.8549	230.014	129.287	229.798
140.000	0.8659	241.645	139.299	241.435
150.000	0.8757	253.136	149.309	252.931

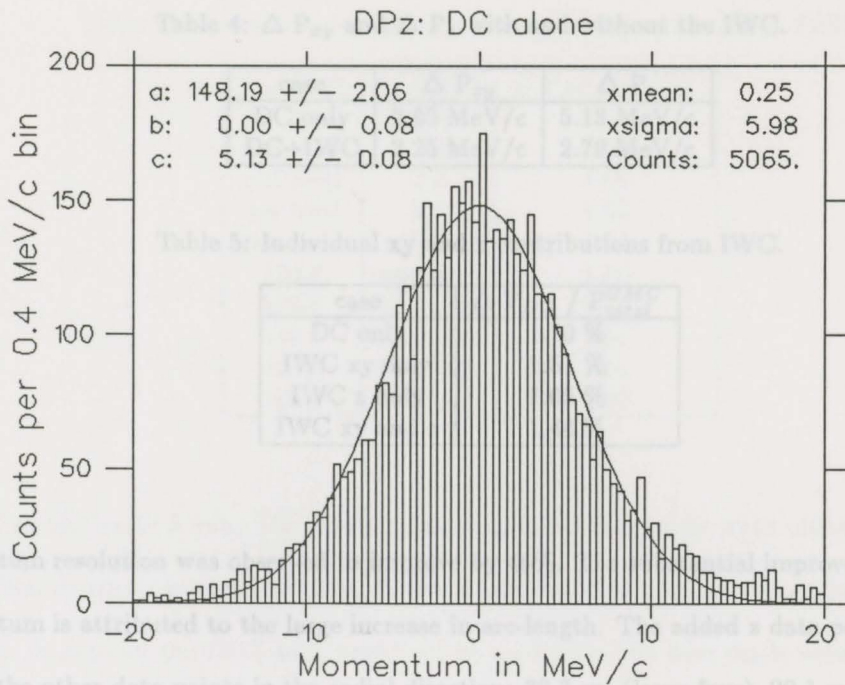


Figure 5: DC minus UMC z momentum.

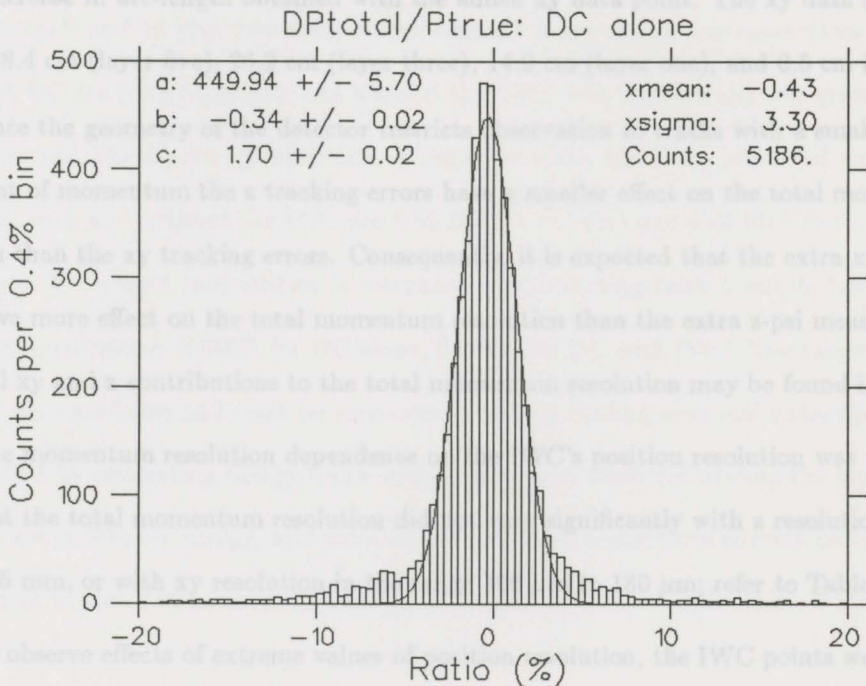


Figure 6: DC minus UMC / UMC total momentum resolution.

Table 4: ΔP_{xy} and ΔP_z with and without the IWC.

case	ΔP_{xy}	ΔP_z
DC only	2.65 MeV/c	5.13 MeV/c
DC+IWC	2.25 MeV/c	2.79 MeV/c

Table 5: Individual xy and z contributions from IWC.

case	$\Delta P_{DC} / P_{total}^{UMC}$
DC only	1.70 %
IWC xy only	1.51 %
IWC z only	1.65 %
IWC xy and z	1.44 %

z-momentum resolution was observed to improve by 46%. The substantial improvement in z-momentum is attributed to the large increase in arc-length. The added z data point is relatively far from the other data points in the radial direction: 32.3 cm (layer four), 20.1 cm (layer two), and 8.5 cm (IWC). The comparatively modest xy-momentum improvement is attributed to the smaller increase in arc-length obtained with the added xy data point. The xy data are radially spaced: 38.4 cm (layer five), 26.2 cm (layer three), 14.0 cm (layer one), and 8.5 cm (IWC).

Since the geometry of the detector restricts observation to tracks with a small longitudinal component of momentum the z tracking errors have a smaller effect on the total momentum resolution than the xy tracking errors. Consequently, it is expected that the extra xy measurement would have more effect on the total momentum resolution than the extra z-psi measurement. The individual xy and z contributions to the total momentum resolution may be found in Table 5.

The momentum resolution dependence on the IWC's position resolution was tested with the result that the total momentum resolution did not vary significantly with z resolution in the range 1 mm to 5 mm, or with xy resolution in the range 100 μm to 180 μm ; refer to Table 6.

To observe effects of extreme values of position resolution, the IWC points were forced into the xy and z fits with position smearing up to 1 mm in xy and 10 cm in z. As illustrated in figures 7 and 8 the total momentum resolutions with IWC reach non-IWC values near xy resolution of 500

Table 6: Momentum resolution versus position resolutions in IWC.

σ_{xy} (μm)	σ_z (mm)	$\Delta P_{DC} / P_{total}^{UMC}$
not used	1.0	1.64
not used	2.0	1.65
not used	3.0	1.65
not used	4.0	1.67
not used	5.0	1.68
100.0	not used	1.50
120.0	not used	1.50
140.0	not used	1.51
160.0	not used	1.51
180.0	not used	1.52

μm and z resolution of 5 mm. The z data was not included in z -psi fit when obtaining xy -resolution dependence and vice versa. These numbers define minimum goals for IWC position resolution. In practice the IWC data would not be used if the fits were made worse; if the IWC point increased the chi-squared per degrees of freedom beyond some threshold value then the IWC point would not be added to the fits.

Figures 9 and 10 illustrate total momentum including energy loss corrections as calculated by KOFIA DC tracking code with and without the IWC. The IWC model was given 2mm z -resolution and 150 micron xy -resolution. From these plots, the UMC predicted momentum resolutions with and without the IWC are 3.55 MeV/c (1.74%) and 4.03 MeV/c (1.97%) respectively. The target contribution is estimated by subtracting table 5 results from the above numbers in quadrature: 0.995% for DC alone, 0.977% for DC with IWC. The target contributions are relatively significant and must be accounted for when dealing with real data; this is accomplished by estimating energy losses within the target when calculating the kinematic variables: range, kinetic energy, and momentum. The final momentum spectra indicate an improvement in the $K\pi^2$ momentum resolution of 12% for Monte Carlo data.

Figure 8: Momentum resolution versus IWC z resolution.

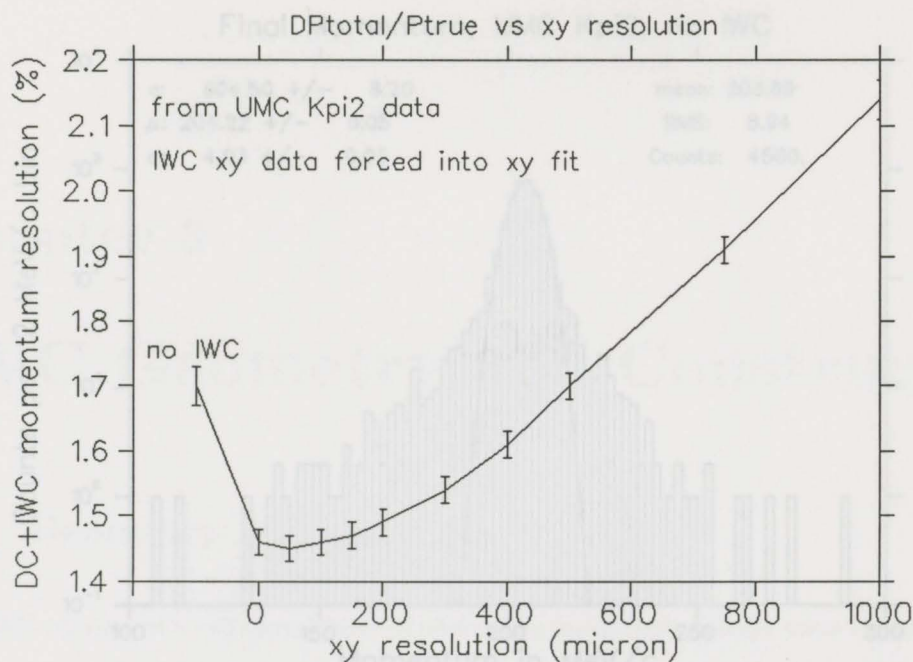


Figure 7: Momentum resolution versus IWC xy resolution.

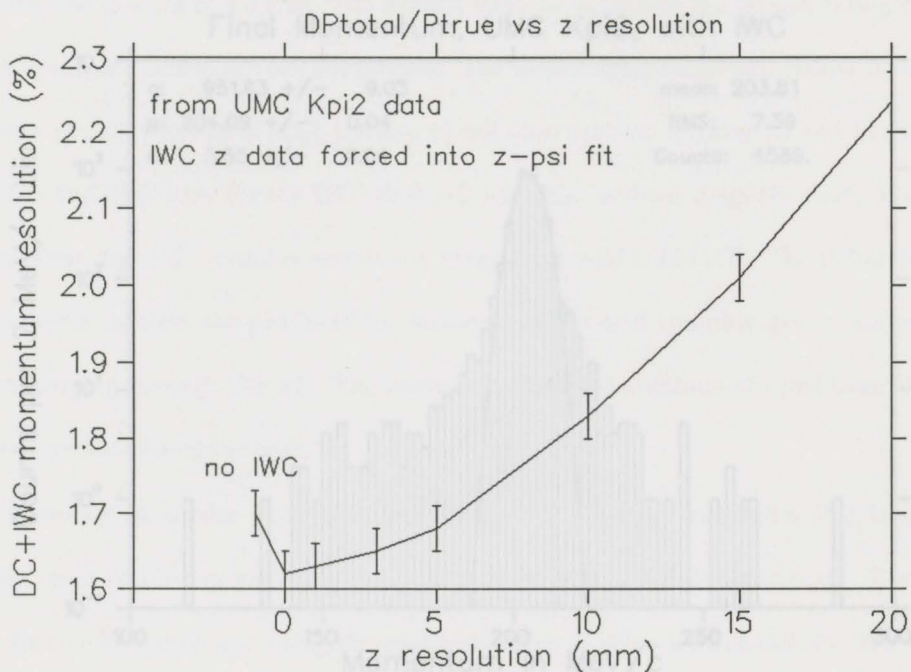


Figure 8: Momentum resolution versus IWC z resolution.

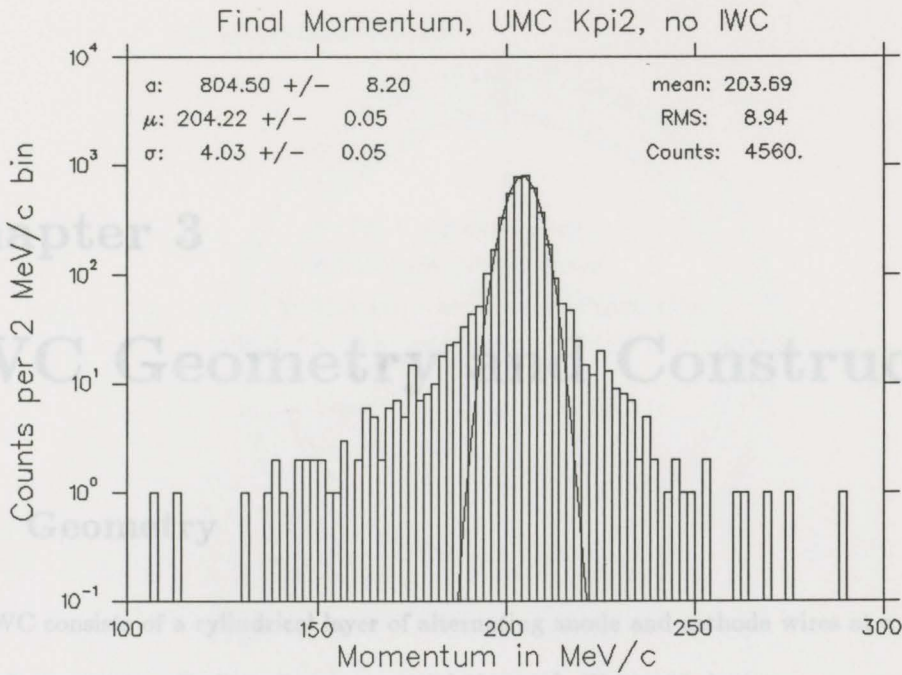


Figure 9: Final UMC $K\pi 2$ momentum for DC alone.

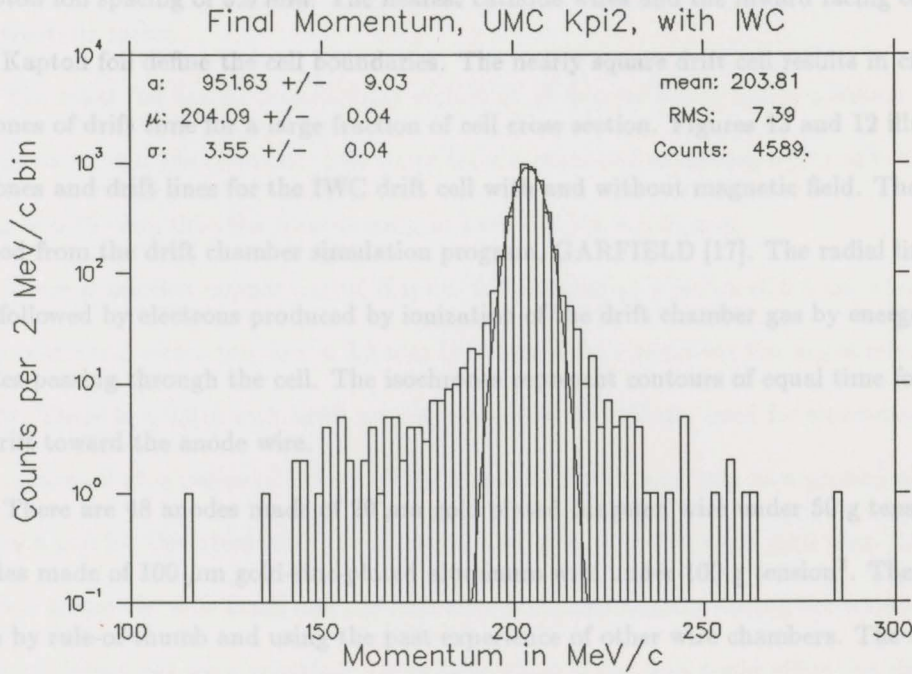


Figure 10: Final UMC $K\pi 2$ momentum for DC and IWC.

Chapter 3

IWC Geometry and Construction

3.1 Geometry

The IWC consists of a cylindrical layer of alternating anode and cathode wires at a radius of 8.5 cm, and concentric cylinders of copper coated Kapton¹. Figure 11 depicts an xy cross section of the IWC. Each drift cell is 28.0 cm long with cathode to anode wire spacing of 5.56 mm and anode to Kapton foil spacing of 5.5 mm. The nearest cathode wires and the inward facing copper surfaces of the Kapton foil define the cell boundaries. The nearly square drift cell results in circular isochrones of drift time for a large fraction of cell cross section. Figures 13 and 12 illustrate isochrones and drift lines for the IWC drift cell with and without magnetic field. These plots were obtained from the drift chamber simulation program, GARFIELD [17]. The radial lines represent paths followed by electrons produced by ionization of the drift chamber gas by energetic charged particles passing through the cell. The isochrones represent contours of equal time for electrons that drift toward the anode wire.

There are 48 anodes made of 20 μm gold plated tungsten wire under 50 g tension and 48 cathodes made of 100 μm gold-zinc-plated aluminum wire under 100 g tension². The tensions were chosen by rule-of-thumb and using the past experience of other wire chambers. The tensions chosen were deemed appropriate to provide a restoring force sufficient to overcome deflections due

¹Kapton is a registered trade mark of the DuPont Corporation

²The wire was obtained from California Fine Wire Company

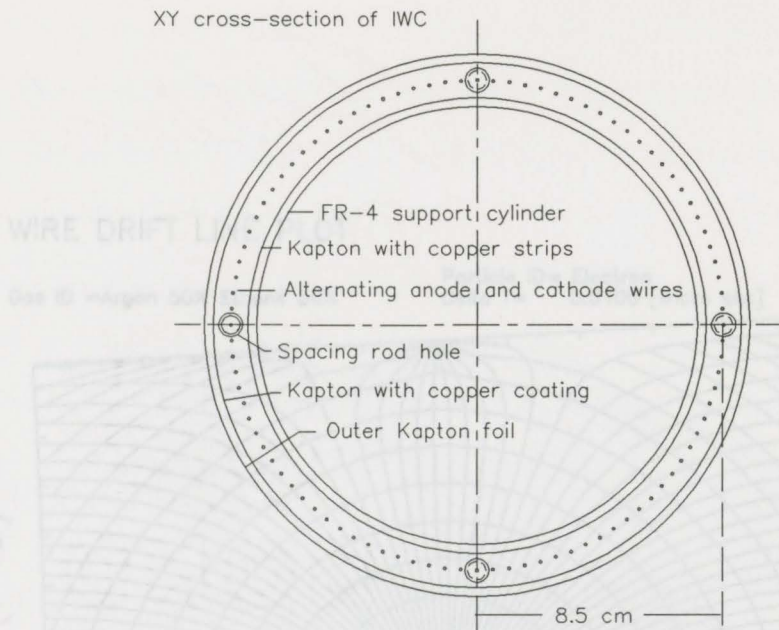


Figure 11: XY cross section of IWC

to electrostatic forces.

The inner foil has 60 copper strips etched at 45 degrees which follow a helical arc wrapping 189 degrees around the chamber. The strips have a measured minimum width of 5.10 mm and spacing of 0.78 mm, thus the strip spacing in z coordinate is 8.32 mm.

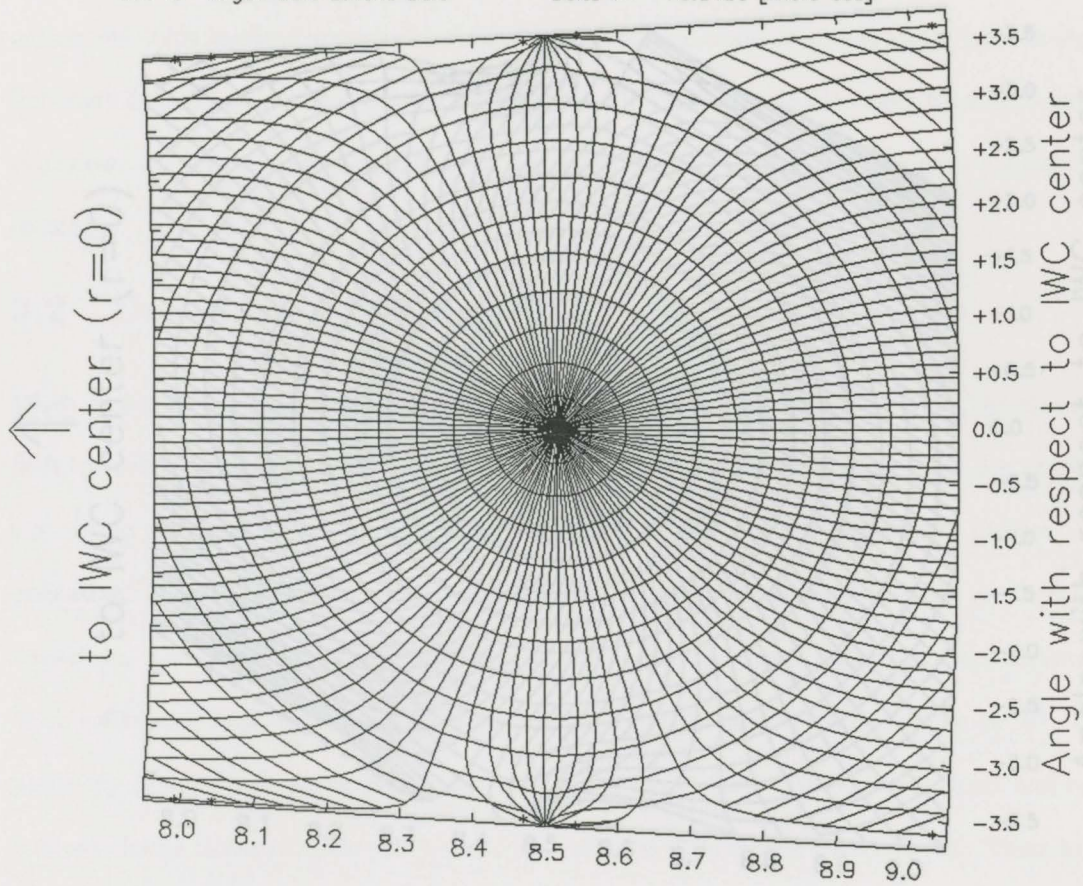
There is another copper coated Kapton foil cylinder at a radius of 9.4 cm which is used as a ground plane and which provides a 3.5 mm thick space for circulating the argon ethane gas mixture. There is a 0.015 inch thick copper coated FR-4³ cylinder used for structural support which is located at a radius of 7.6 cm. This support cylinder also acts as a ground plane and provides a gap for the circulating gas mixture. The inner and outer gas gaps keep the pressure difference across the foils small and the foils were tensioned slightly during the construction process so that no deflections were expected. Large deflections of the foils could affect the electric field and consequently degrade the performance of the drift cells; for example, with outward deflection the

³FR-4 is a universal trade name for this particular glass-epoxy composite; the supplier was Micarta

WIRE DRIFT LINE PLOT

Gas ID = Argon 50% Ethane 50%

Particle ID = Electron
Delta T = 0.0100 [Micro sec]



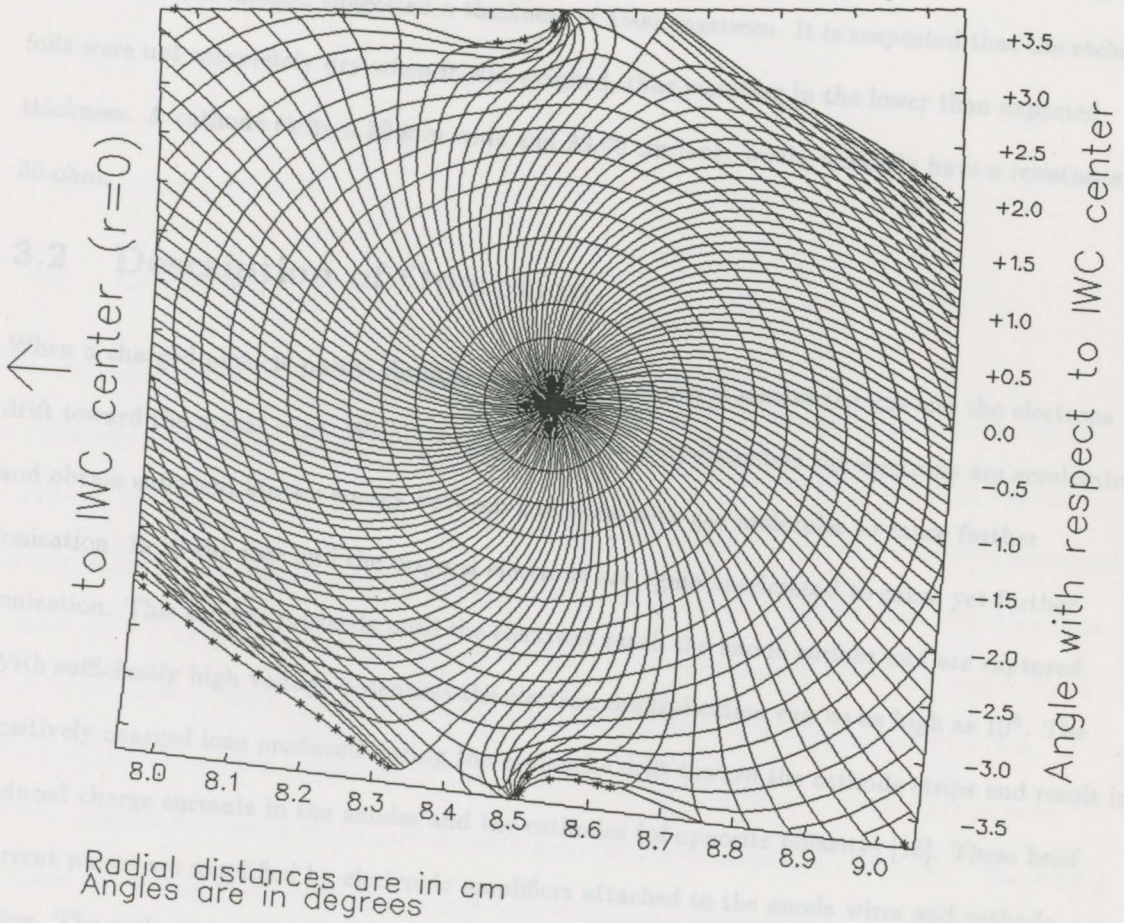
Radial distances are in cm
Angles are in degrees

Figure 12: Isochrones and Drift Lines with $B = 0$ kG and IWC voltage = 2.0 kV

WIRE DRIFT LINE PLOT

Gas ID = Argon 50% Ethane 50%

Particle ID = Electron
Delta T = 0.0100 [Micro sec]



Radial distances are in cm
Angles are in degrees

Figure 13: Isochrones and Drift Lines with $B = 10$ kG and IWC voltage = 2.0 kV

*Deposition was done by Andrew Flinn

field would be lower near $z = 0$ than at $z = \pm 14\text{cm}$, resulting in different isochrones for different z .

The film was 2000 angstrom ($2 * 10^{-7}$ meter) of vacuum deposited copper on $50\ \mu\text{m}$ thick Kapton⁴. The resistance of thin strips of the foil indicated the thickness was around 1000 angstrom. It is believed that non-conducting oxide layers are responsible for the lower resistance derived measurement. Sheets of foil, 8.5 cm by 11 cm, were weighed before and after etching the copper off. This method suggested a thickness of 1500 angstrom. It is suspected that the etched foils were not completely dry when it was weighed, thus resulting in the lower than expected thickness. A cathode strip, 5.10 mm wide and 39.60 cm long, would typically have a resistance of 30 ohm.

3.2 Description of Operation

When a charged particle passes through the drift cell region it ionizes the gas and the electrons drift toward the anode wire. Within a radius of a few wire diameters the electrons are accelerated and obtain sufficient kinetic energy between collisions with gas molecules to cause further ionization. Both the new and the original electrons are again accelerated to cause yet further ionization. This process proceeds until the electrons reach the anode surface and are captured. With sufficiently high voltage potentials the electron multiplication can be as high as 10^5 . The positively charged ions produced during the avalanche drift toward the cathode strips and result in induced charge currents in the anodes and the cathodes (of opposite polarity) [18]. These brief current pulses are amplified by electronic amplifiers attached to the anode wires and cathode strips. The cathode strips nearest the the anode wire have a larger induced charge and consequently the amplified voltage signals can be used to estimate the position of the avalanche.

Measuring the time of the avalanche with respect to estimated time of passage of original particle trajectory allows an estimate of radial distance from the trajectory to the wire. The drift chamber gas, argon/ethane/ethanol, yields a relatively constant electron drift velocity for

⁴Deposition was done by Andus Films High Purity Gases Canada Incorporated

moderate to high electric field potentials (figure 14, from GARFIELD), thus resulting in a linear relation between distance and drift time. The anode drift distance is used in the xy track fits.

The z positions given by the wire and cathode intersections are weighted by relative magnitude of induced charge and averaged to yield a z-position for the avalanche position. Since there is no z-component for electric field between strips and anodes, the drifting electrons are presumed not to travel in z direction, thus the weighted average z position is equated with the z position of the charged particle trajectory at the point of primary ionization. This weighted average z position is used in the z-psi fits, where the angle psi is calculated from the xy coordinate of the primary ionization.

3.3 Construction

The cathode strips were produced by etching unwanted copper from copper-coated Kapton film. In a clean and dust free environment, the foils were taped to a G-10⁵ sheet (100 cm by 150 cm by 0.125 cm) for easier handling. They were then airbrushed (three coats) with a positive photoresist⁶ and dried for eight hours in a well ventilated, dark, and clean environment. The foils were then exposed to UV light with a mask on top of the foil which cast shadows where the copper strips were to be formed. After exposure the foils were then placed in a developing solution that dissolved the UV treated photoresist⁷. The solution was maintained at room temperature to prevent possible fracturing of the surface coating due to rapid temperature changes. After rinsing in water and drying in ambient air, the foils were etched in a diluted ferric chloride solution⁸, then rinsed and dried again. At this stage the foils were visually and electrically inspected for shorts between strips due to dust shadows, then repaired by scratching photoresist off and etching exposed copper with a Q-TIP⁹. Finally the foils were re-exposed to UV light and the remaining

⁵G-10 is a universal trade name for this particular glass-epoxy composite; the supplier was Micarta

⁶MG Chemicals # 416 diluted 1:1 with MG Chemicals # 417

⁷MG Chemicals # 418 diluted 1:8 with water

⁸MG Chemicals # 415 diluted 1:5 with water

⁹Q-TIP is a registered trade mark of Chesebrough Ponds Canada Incorporated

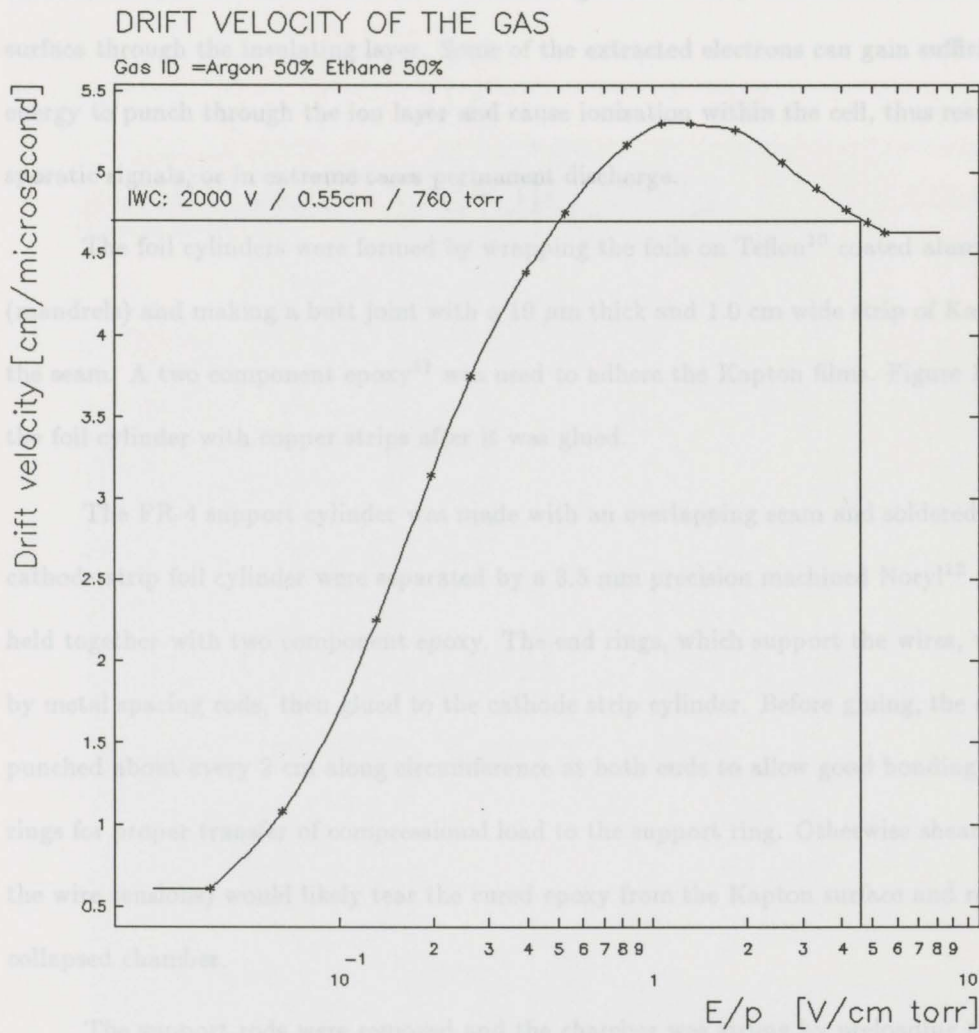


Figure 14: Drift velocity for Argon/Ethane 50/50 gas (from GARFIELD)

¹⁰Teflon is a registered trade mark of the DuPont Corporation

¹¹The epoxy used was Araldite by CIBA-GENEY

¹²Noryl is a registered trade mark of General Electric

photoresist was dissolved in the developer. Finally, the organic residuals were wiped from the copper surface with acetone. The residuals, if not removed, could contaminate the drift cell gas or form insulating layers on the surfaces of the cathodes. Of particular concern is the Malter effect whereby the positive ions collect on the insulating surface and pull electrons from the copper surface through the insulating layer. Some of the extracted electrons can gain sufficient kinetic energy to punch through the ion layer and cause ionization within the cell, thus resulting in sporadic signals, or in extreme cases permanent discharge.

The foil cylinders were formed by wrapping the foils on Teflon¹⁰ coated aluminum cylinders (mandrels) and making a butt joint with a 10 μm thick and 1.0 cm wide strip of Kapton overlaying the seam. A two component epoxy¹¹ was used to adhere the Kapton films. Figure 15 illustrates the foil cylinder with copper strips after it was glued.

The FR-4 support cylinder was made with an overlapping seam and soldered. The ring and cathode strip foil cylinder were separated by a 3.5 mm precision machined Noryl¹² plastic ring and held together with two component epoxy. The end rings, which support the wires, were held rigid by metal spacing rods, then glued to the cathode strip cylinder. Before gluing, the strip foil was punched about every 2 cm along circumference at both ends to allow good bonding between end rings for proper transfer of compressional load to the support ring. Otherwise shear forces (due to the wire tensions) would likely tear the cured epoxy from the Kapton surface and result in a collapsed chamber.

The support rods were removed and the chamber was strung by preloading the endrings with four symmetric spaced 150 micron berillium copper wires with 100 grams tension, then the 100 micron cathode wires were strung and the pretensioning wires removed. The anode wires were put in last. The method of stringing was as follows: place chamber in upright position; set all top

¹⁰Teflon is a registered trade mark of the DuPont Corporation

¹¹The epoxy used was Araldite by CIBA-GEIGY

¹²Noryl is a registered trade mark of General Electric

Table 7: Measured wire densities.

wire type	wire diameter	wire length	wire volume	wire density
Au-W	20 μm	280.72 cm	0.000178 cm ³	19.30 g/cm ³
Au-Zn-Al	100 μm	150.09 cm	0.000125 cm ³	1.50 g/cm ³

pins in the Noryl end ring; feed the wire through top pin, top end ring, wire region, bottom end ring, and bottom crimp pin; suspend weight from the wire to provide tension; set the bottom crimp

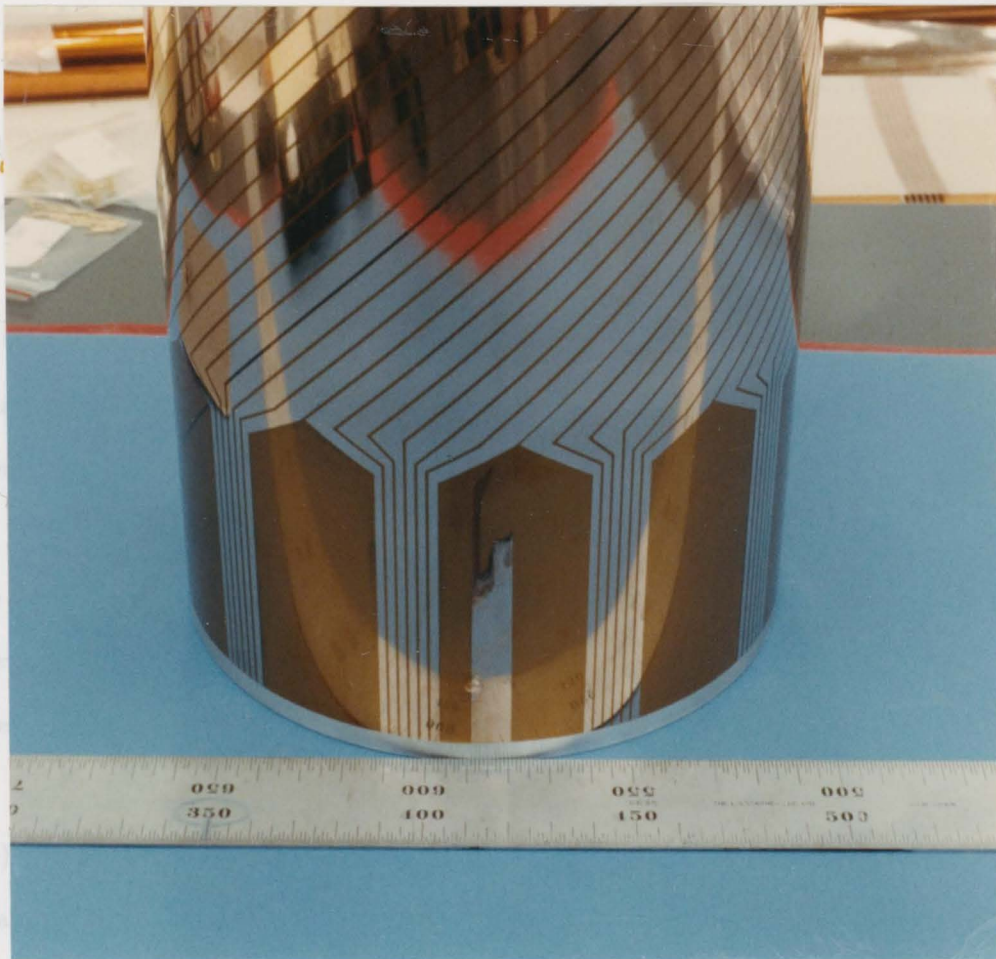


Figure 15: Copper strips on inner foil

¹²Corros Dope is a trade name; it was supplied by GC Electronics.

¹³Flexiglass is a registered trade mark of Holm and Haas Canada Incorporated.

¹⁴The manufacturer was Wright Capacitors Incorporated.

Table 7: Measured wire densities.

wire type	wire diameter	wire length	wire mass	wire density
Au-W	20 μm	280.75 cm	0.0164 gm	18.59 g/cm^3
Au-Zn-Al	100 μm	150.00 cm	0.0430 gm	3.650 g/cm^3

pins in the Noryl end ring; feed the wire through top pin, top end ring, active region, bottom end ring, and bottom crimp pin; suspend weight from the wire to provide tension; set the bottom crimp pin in the bottom end ring; crimp the top then the bottom pins; trim access wire.

After stringing was completed, the wire tensions were measured with a tension meter. The chamber was left for 24 hours to check for wire creep due to poor crimping and some wires were replaced.

The outer foils were epoxied in place with each foil and end ring layer taking 24 hours to allow for epoxy curing time. Then the wire tensions were measured again. Table 7 contains the measured wire densities and table 8 contains the final measured IWC wire tensions. Figure 16 illustrates the measured wire tensions.

A chain of 100 kohm resistors was used to connect the anodes together on the upstream end of the chamber. The resistors and leads were painted with Corona Dope¹³ (an electrical insulator) to prevent arcing to the cathode crimp pins. This high voltage distribution network was protected and sealed by a molded Plexiglass¹⁴ shield.

The downstream side cathode crimp pins were connected to a circular printed circuit board (PCB) via connector pins soldered to 20 AWG solid bus-wire. The downstream anode crimp pins were also connected to the PCB, but via 1000 pF 4 kV decoupling capacitors. Ceramic chip decoupling capacitors¹⁵ (for isolating the high voltage from the electronics) were soldered to connector pins on one side and bus-wire on the other, then painted with Corona Dope. The cathode leads were coated with heat shrink, thus minimizing chance of arcing between alternating

¹³Corona Dope is a trade name; it was supplied by GC Electronics

¹⁴Plexiglass is a registered trade mark of Rohm and Hass Canada Incorporated

¹⁵The manufacturer was Wright Capacitors Incorporated

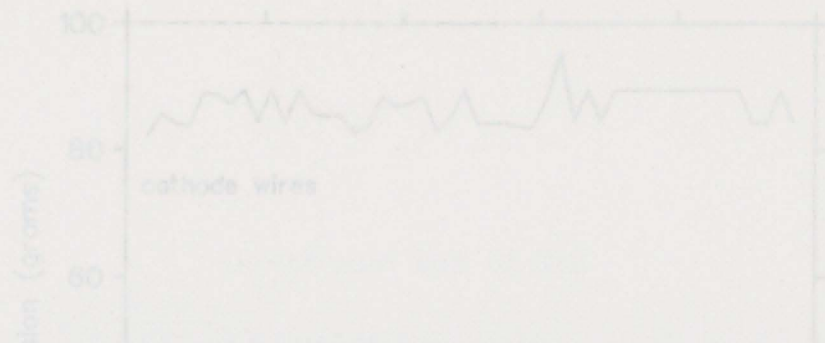


Table 8: IWC wire tensions from tension meter, February 23/24, 1991.

Chan	meter	mass	Chan	meter	mass	Chan	meter	mass	Chan	meter	mass
C-1	3.34	82.1	C-13	3.27	85.7	C-25	3.30	84.2	C-37	3.20	89.5
C-2	3.27	85.7	C-14	3.28	85.2	C-26	3.30	84.2	C-38	3.20	89.5
C-3	3.30	84.2	C-15	3.27	85.7	C-27	3.30	84.2	C-39	3.20	89.5
C-4	3.31	83.6	C-16	3.33	82.6	C-28	3.31	83.6	C-40	3.20	89.5
C-5	3.21	88.9	C-17	3.31	83.6	C-29	3.31	83.6	C-41	3.20	89.5
C-6	3.21	88.9	C-18	3.22	88.4	C-30	3.23	87.8	C-42	3.20	89.5
C-7	3.24	87.3	C-19	3.25	86.8	C-31	3.10	95.4	C-43	3.20	89.5
C-8	3.20	89.5	C-20	3.24	87.3	C-32	3.29	84.7	C-44	3.20	89.5
C-9	3.30	84.2	C-21	3.22	88.4	C-33	3.20	89.5	C-45	3.30	84.2
C-10	3.20	89.5	C-22	3.32	83.1	C-34	3.29	84.7	C-46	3.30	84.2
C-11	3.30	84.2	C-23	3.28	85.2	C-35	3.20	89.5	C-47	3.20	89.5
C-12	3.20	89.5	C-24	3.20	89.5	C-36	3.20	89.5	C-48	3.30	84.2
A-1	2.27	36.2	A-13	2.11	41.9	A-25	2.24	37.2	A-37	2.63	27.0
A-2	2.75	24.7	A-14	2.39	32.7	A-26	2.20	38.6	A-38	2.59	27.8
A-3	2.22	37.9	A-15	2.25	36.9	A-27	2.88	22.5	A-39	2.24	37.2
A-4	2.18	39.3	A-16	2.55	28.7	A-28	2.26	36.6	A-40	2.80	23.8
A-5	2.60	27.6	A-17	2.84	23.2	A-29	2.26	36.6	A-41	2.20	38.6
A-6	2.90	22.2	A-18	2.25	36.9	A-30	2.50	29.9	A-42	2.45	31.1
A-7	2.21	38.2	A-19	2.72	25.2	A-31	2.12	41.5	A-43	2.48	30.4
A-8	2.10	42.3	A-20	2.53	29.2	A-32	2.52	29.4	A-44	2.70	25.6
A-9	2.20	38.6	A-21	2.90	22.2	A-33	2.33	34.4	A-45	2.16	40.0
A-10	2.20	38.6	A-22	2.66	26.4	A-34	2.85	23.0	A-46	2.47	30.6
A-11	2.40	32.4	A-23	2.20	38.6	A-35	2.47	30.6	A-47	2.96	21.3
A-12	2.28	35.9	A-24	2.97	21.2	A-36	2.89	22.4	A-48	2.23	37.6

pins which were then connected to preamp pins at the same circuit board using...

On the circuit board the various signals were routed to single row Amphenol[®] connectors to which the preamplifiers were connected.

Figure 17 illustrates the end-rings and pins at the up-stream end of the IWC. Figure 18 illustrates the capacitors and cathode strip connections at the downstream end of the IWC.

[®]Amphenol Canada Corporation

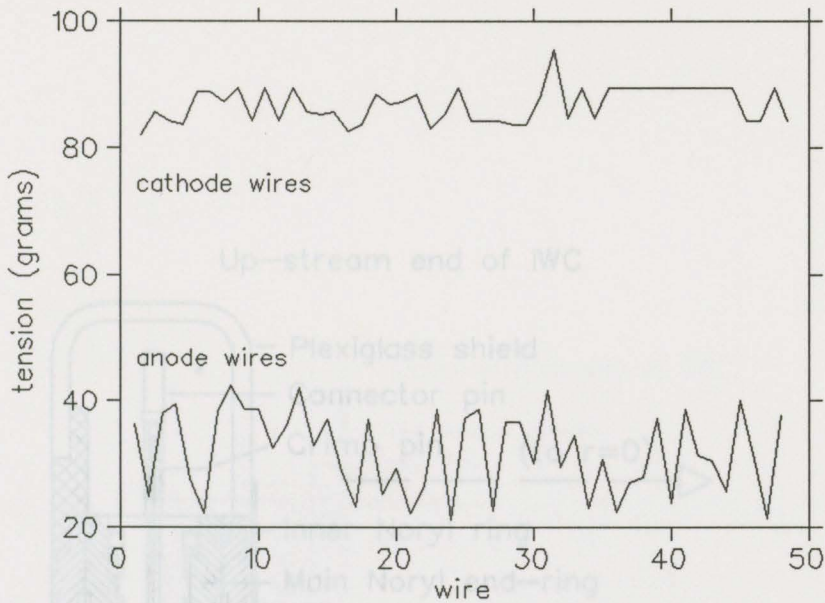


Figure 16: Measured wire tensions

anode and cathode pins. Care was taken to ensure that no finger prints were left on the coated capacitor surfaces, so that no arcing between capacitor leads would occur. High voltage was supplied by soldering an insulated multi-strand wire to the chamber side of one decoupling capacitor.

The cathode strips were tapered and extended downstream of the chamber where they were epoxied and soldered to a thin G-10 support ring. Copper traces on the ring connected the strips to pins which were then connected to receptor pins in the same circular printed circuit board above.

On the circuit board the various signals were routed to single row Amphenol¹⁶ connectors to which the preamplifiers were connected.

Figure 17 illustrates the end-rings and pins at the up-stream end of the IWC. Figure 18 illustrates the capacitors and cathode strip connections at the downstream end of the IWC.

¹⁶Amphenol Canada Corporation

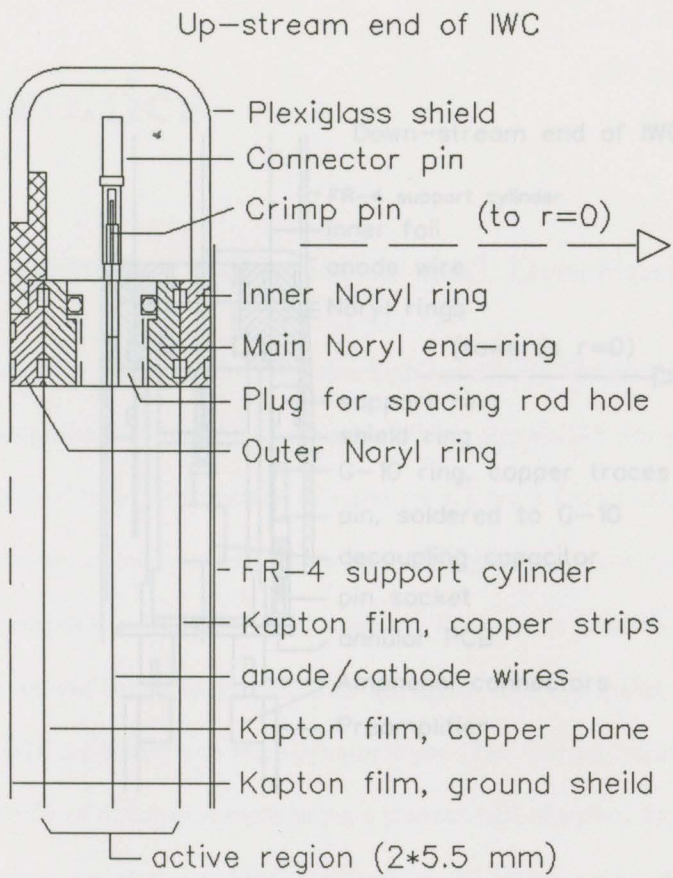


Figure 16: Close up view of down stream end of IWC

Figure 17: Close up view of up stream end of IWC

Chapter 4

Electronics

4.1 Preamplifier

A two-stage amplifier was used as a preamplifier together and two of the preamplifier modules provide low noise and 100 feet of RG174 cable

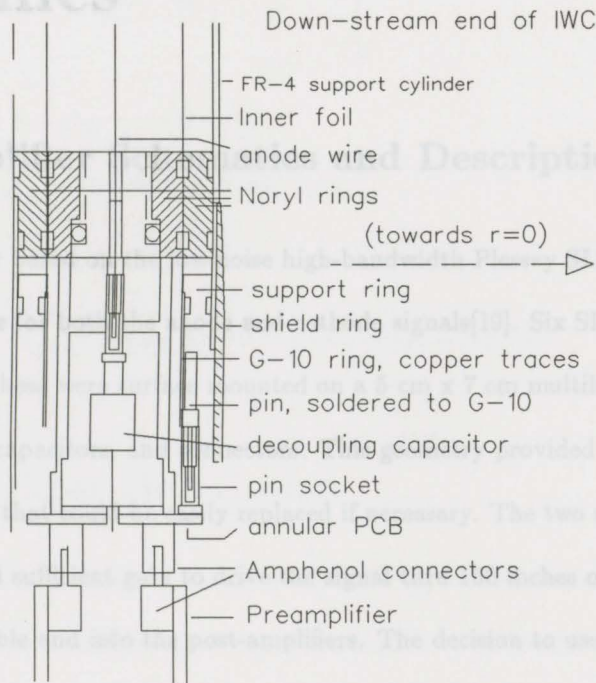


Figure 18: Close up view of down stream end of IWC

The first stage, as illustrated in figure 18, is configured as a common base amplifier and the second stage as a common emitter. The first stage has a voltage gain of -5 and the second has a voltage gain of +5. The resulting amplifier has a measured voltage gain of 28 db for 50ns wide pulses, a noise level of 1.5 mV peak-to-peak, a saturated output voltage of 150 mV peak-to-peak, and a total power consumption of 125 mW at the chosen operating voltage of 6 volts.

¹Alpha Wire Corporation

Chapter 4

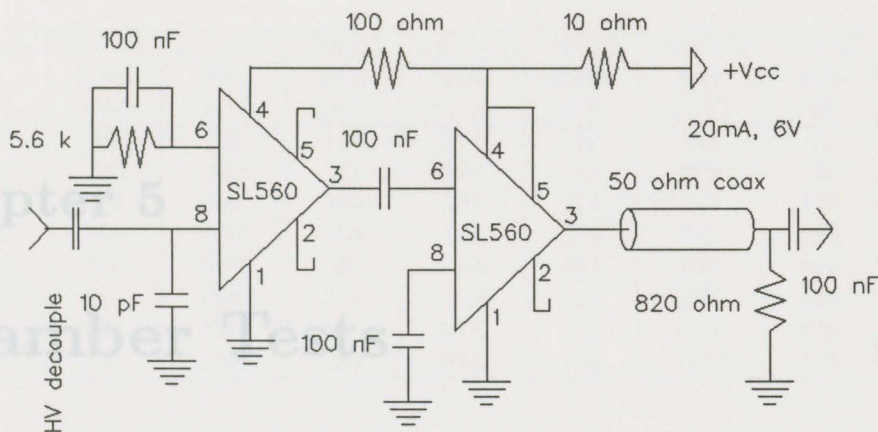
Electronics

4.1 Preamplifier Schematics and Description

A two-stage amplifier based on the low-noise high-bandwidth Plessey SL560 integrated circuit was used as a preamplifier for both the anode and cathode signals[19]. Six SL560 dies were packaged together and two of these were surface mounted on a 5 cm x 7 cm multilayer printed circuit board along with resistors, capacitors, and connectors. This geometry provided a slim fit with preamplifier modules that could be easily replaced if necessary. The two stage design was chosen to provide low noise and sufficient gain to drive the signal thru 150 inches of Alpha 9374 cable¹ and 100 feet of RG174 cable and into the post-amplifiers. The decision to use a two-stage pre-amplifier came from a study of different designs using a similar drift chamber. It was found that the higher gain of a two stage design was needed to provide useful cathode strip efficiencies for nominal high voltages.

The first stage, as illustrated in figure 19, is configured as a common base amplifier and the second stage as a common emitter. The first stage has a voltage gain of -5 and the second has a voltage gain of +5. The resulting amplifier has a measured voltage gain of 28 db for 50ns wide pulses, a noise level of 1.5 mV peak-to-peak, a saturated output voltage of 150 mV peak-to-peak, and a total power consumption of 120 mW at the chosen operating voltage of 6 volts.

¹Alpha Wire Corporation



1) noise 1.5 mV p/p

2) max output 150 mV p/p

Figure 19: IWC preamplifier schematic.

4.2 Postamplifier Description

A detailed description of the post amplifier electronics may be found in reference [9]. A brief description is as follows. The input lines (from preamplifiers) are connected to a matching transformer. The output from the transformer is split into an analog branch and a digital branch. The analog branch consists of a differential amplifier followed by a common-emitter line driver. The digital branch consists of a differential amplifier, a comparator (for threshold discrimination), and an ECL (Emitter Coupled Logic) line driver.

The cathode strip signals were polarity reversed at the matching transformer input and the gains of the output stage were boosted by a factor of three to reduce the anode cathode gain difference. The amplified analog signals were read by LeCroy 1882F Fast Bus ADCs (Analog to Digital Converter), and the ECL output of the discriminator were fed to a LeCroy 1879 Fast Bus multihit TDCs (Time to Digital Converter) [20].

Table 9: Fe⁵⁵ pulse heights vs HV. Ar/Fe 22/56, 200cc/min.

Voltage (kV)	C10.S1 strip (mV)	A06.W3 wire (mV)	C08.S1 strip (mV)	A04.W3 wire (mV)	C05.S2 strip (mV)	A02.W3 wire (mV)	C02.S2 strip (mV)	A08.W5 wire (mV)
1.75	80	225	112	224	100	360	82	225
1.80	130	260	161	262	148	370	130	260
1.85	274	355	240	342	225	540	109	311
1.90	274	800	354	730	304	775	280	730
1.95	365	1075	460	1060	432	880	414	970
2.00	510	1320	630	1270	670	1240	550	1200
2.05	590	1400	690	1400	690	1370	675	1480
2.10	690	1750	830	1600	940	1520	825	1600

Chapter 5

Chamber Tests

Table 10: IWC current vs high voltage

After construction of the IWC, gas leaks were found and patched, then the high voltage was raised slowly (with argon/ethane gas flowing) and then maintained at 2.0 kV for a period of 24 hours. Once it was established that the chamber could hold the potential all anode and cathode channels at the post amplifier outputs were checked for signals with 5.89 keV photons from an Fe⁵⁵ source. The continuity of the cathode strips was tested by collimating the Fe⁵⁵ source and aiming the photons at the upstream end of the chamber. The photons caused ionization of the chamber gas and the resulting signals on each cathode strip were observed. Figures 21 and 22 illustrate typical anode and cathode pulse heights for the Fe⁵⁵ source. Figure 20 and table 9 show measured Fe⁵⁵ pulse heights from anodes and strips as a function of high voltage.

Without radiation sources the IWC was observed to draw 50 nA current from the high voltage supply at all voltages above 100 volts. With the Fe⁵⁵ source the IWC drew 50 nA at 1.8 kV and 90 nA at 2.0 kV.

At BNL the current draw versus high voltage was observed during normal E787 running conditions. The AGS was providing $3.5 - 4.0 \times 10^5$ stopped kaons per beam spill where each spill was of duration, 1.5 seconds, and interval, 3.0 seconds. Table 10 contains the peak current as measured by the IWC high voltage supply for a range of high voltages. Between the spills the current dropped below 100 nA, thus demonstrating that the so called "dark current" was

Table 9: Fe⁵⁵ pulse heights vs HV. Ar/Et 50/50, 100cc/min.

Voltage (kV)	C10.S4 strip (mV)	A06.W3 wire (mV)	C08.S1 strip (mV)	A04.W3 wire (mV)	C05.S2 strip (mV)	A02.W2 wire (mV)	C02.S2 strip (mV)	A08.W5 wire (mV)
1.75	86	225	112	224	100	240	92	225
1.80	130	360	161	362	148	370	130	350
1.85	204	556	240	562	225	540	199	514
1.90	274	800	354	790	304	775	280	730
1.95	388	1075	460	1050	452	990	414	970
2.00	510	1330	640	1270	570	1240	550	1230
2.05	700	1570	745	1400	690	1370	675	1480
2.10	890	1700	880	1600	940	1530	825	1660

Table 10: IWC current vs high voltage

Voltage (kV)	Peak Current (μ A)
1.50	0.5
1.60	1.5
1.70	4.5
1.75	7.5
1.80	10
1.85	13
1.90	20
1.95	30
2.00	40
2.05	60

consistent with the Fe⁵⁵ measurements and was negligible for the nominal high voltage of 1.9 kV.

A large dark current would be indicative of a chamber failing due to continuous discharge.

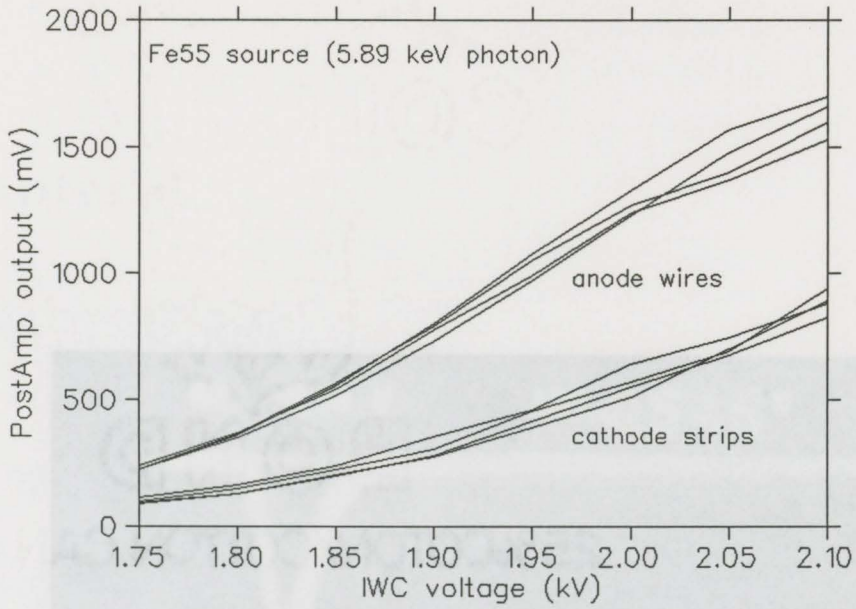


Figure 20: Fe⁵⁵ pulse height vs voltage

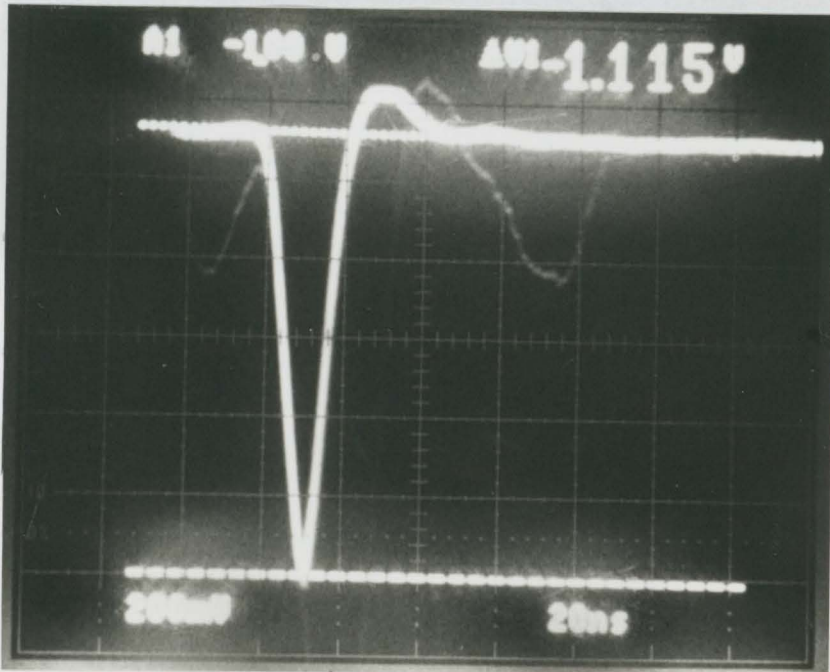


Figure 21: Typical Fe⁵⁵ pulse height on anode wire.

Chapter 6

Calibration

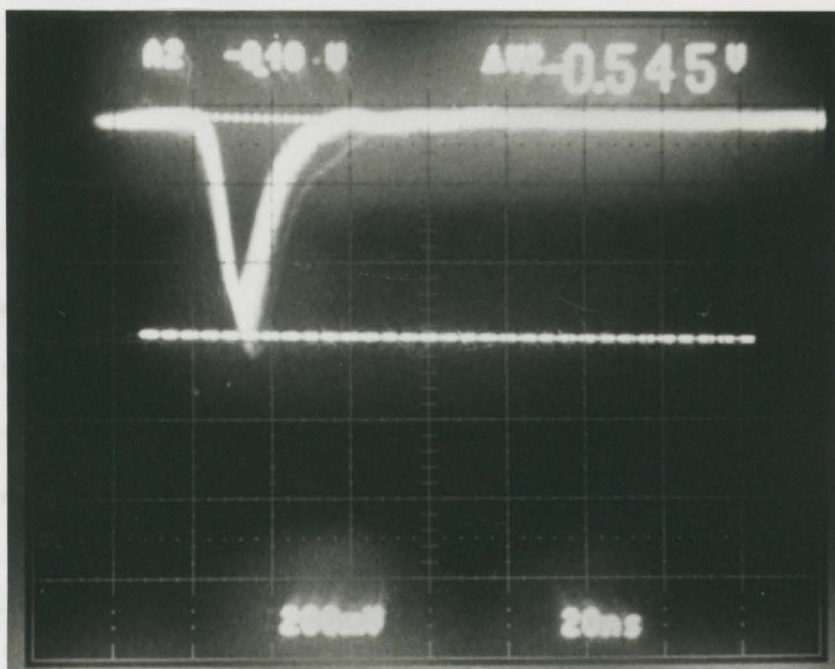


Figure 22: Typical Fe^{55} pulse height on cathode strip.

The ADC zero pedestal was determined, as for the DC ADC's, by using a 50 ns pulse in the E787 trigger system. The pedestal was determined by fitting a Gaussian to the leading edge of the pulse. The values measured were due to voltage effects (from pre and post amplifiers) as observed at the inputs to the 16BITBUS ADC modules. These zero pedestals are used by SLAC Scanner Processor (SSP) modules (one in each 16BITBUS crate) to reject noisy data, but are only subtracted from the data during offline analysis. It was found that during the 1987 run the pedestals shifted less than 5%.

The relative gains of the ADCs were obtained by fitting curves to the pedestal subtracted ADC data. For the anode channels, the anode closest to the expected anode hit (from DC

Chapter 6

Calibration

6.1 Time to Digital Converters

The TDC time offsets, specific to each signal channel, were obtained by fitting the leading edges of the TDC spectra. First each spectrum was smoothed, then the time corresponding to 1/3 peak height was used as a starting value for an iterative method of fitting the leading edge with the error function. This same method was used to derive the starting values for drift chamber TDC offsets. Figures 23 and 24 illustrate the leading edge fits of an anode and a cathode spectrum.

6.2 Analog to Digital Converters

The ADC zero pedestal levels were determined, as for the DC ADC's, by using a 100 Hz pulser in the E787 trigger system to simulate event triggers when there was no beam incident on the detector. The values measured were due to voltage offsets (from pre and post amplifiers) as observed at the inputs to the FASTBUS ADC modules. These zero pedestals are used by SLAC Scanner Processor (SSP) modules (one in each FASTBUS crate) to reject zeros in data, but are only subtracted from the data during offline analysis. It was found that during the 1991 run the pedestals shifted less than 5%.

The relative gains of the ADCs were obtained by fitting curves to the pedestal subtracted ADC data. For the anode channels, the anode closest to the expected anode hit (from DC

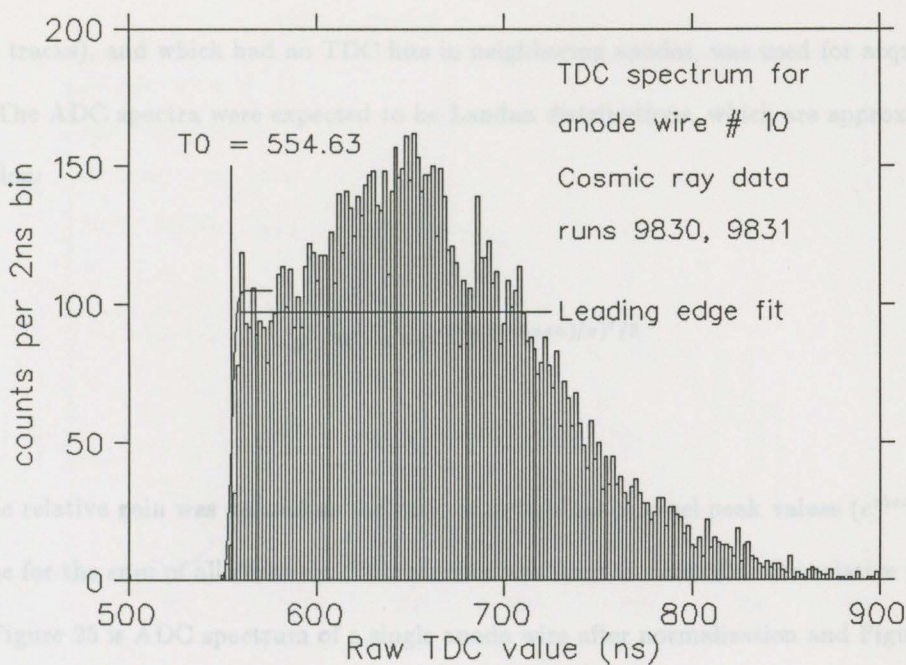


Figure 23: Sample anode wire TDC spectrum.

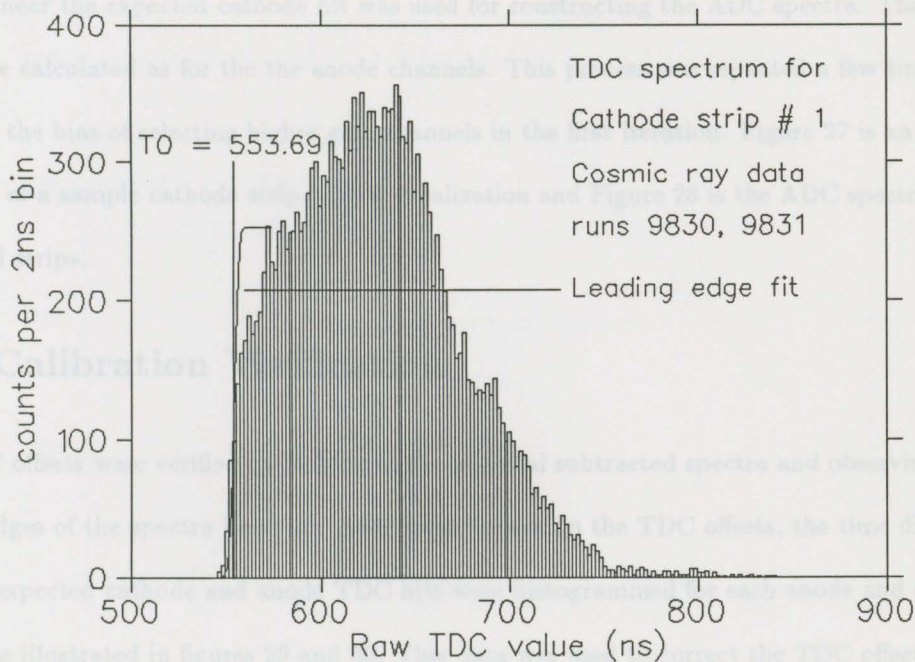


Figure 24: Sample cathode strip TDC spectrum.

projected tracks), and which had no TDC hits in neighboring anodes, was used for acquiring ADC spectra. The ADC spectra were expected to be Landau distributions, which are approximated by the equation:

$$y = a * e^{-((\ln x - \text{mean})/\sigma)^2/2} \quad (5)$$

The relative gain was defined as the ratio of individual channel peak values (e^{mean}) over the peak value for the sum of all channels. This number was used to normalize the relative gains of the anodes. Figure 25 is ADC spectrum of a single anode wire after normalization and Figure 26 is the ADC spectrum for the sum of all anodes.

For the cathode channels, the cathode with the maximum ADC value in the cluster of cathodes near the expected cathode hit was used for constructing the ADC spectra. The relative gains were calculated as for the the anode channels. This process was repeated a few times to overcome the bias of selecting higher gain channels in the first iteration. Figure 27 is an ADC spectrum of a sample cathode strip after normalization and Figure 28 is the ADC spectrum for the sum of all strips.

6.3 Calibration Verification

The TDC offsets were verified by looking at the pedestal subtracted spectra and observing that the leading edges of the spectra lined up. As a refined check on the TDC offsets, the time difference between expected cathode and anode TDC hits were histogrammed for each anode and cathode channel as illustrated in figures 29 and 30. This data was used to correct the TDC offsets for each channel. Figures 31, 32, 33, and 34 demonstrate the improvement in the "c-a" (strip minus anode) timing for $K\pi^2$ data. Improvements in position resolution and momentum resolution were also

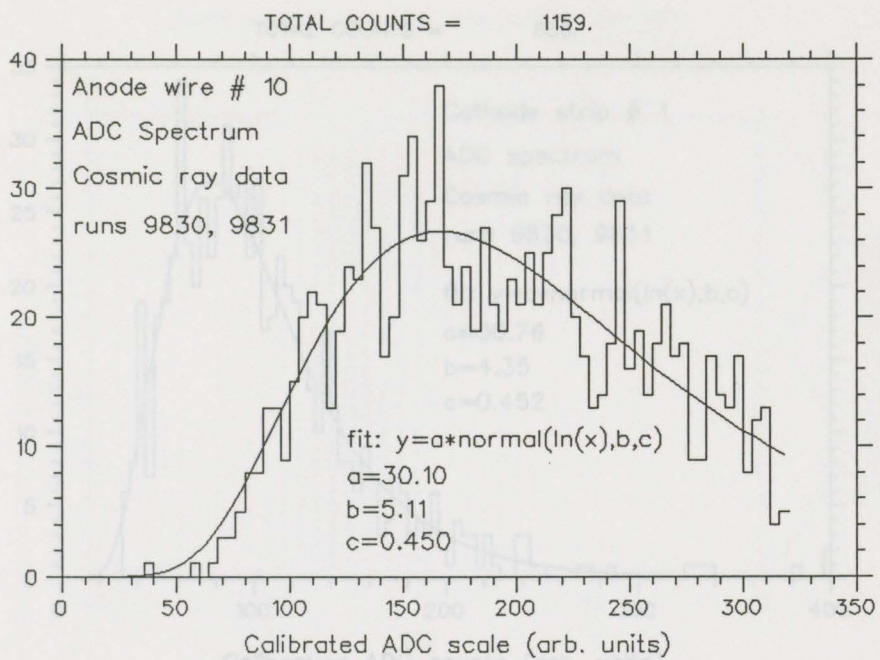


Figure 25: Example anode wire ADC spectrum.

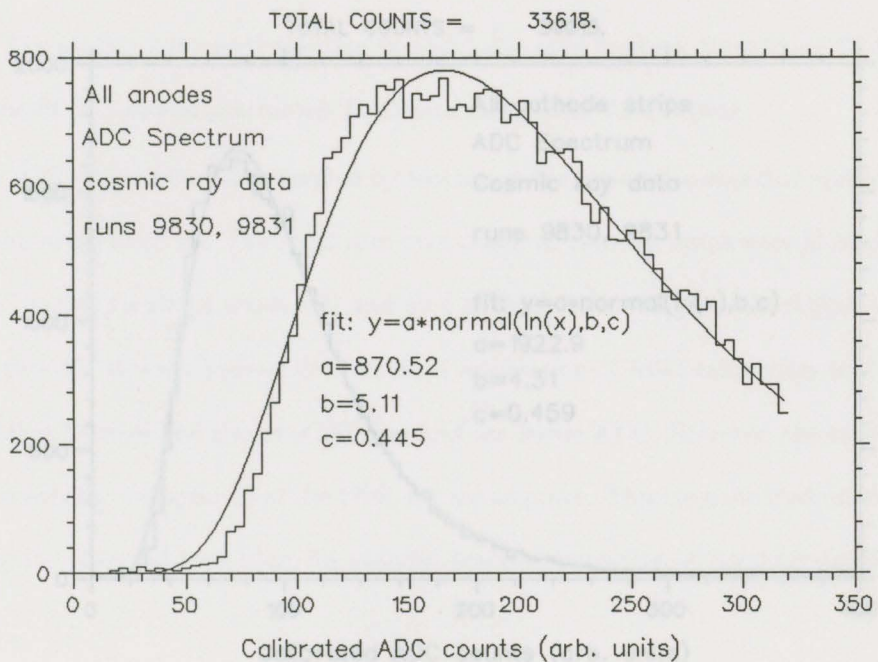


Figure 26: Sum of anode wire ADC spectra.

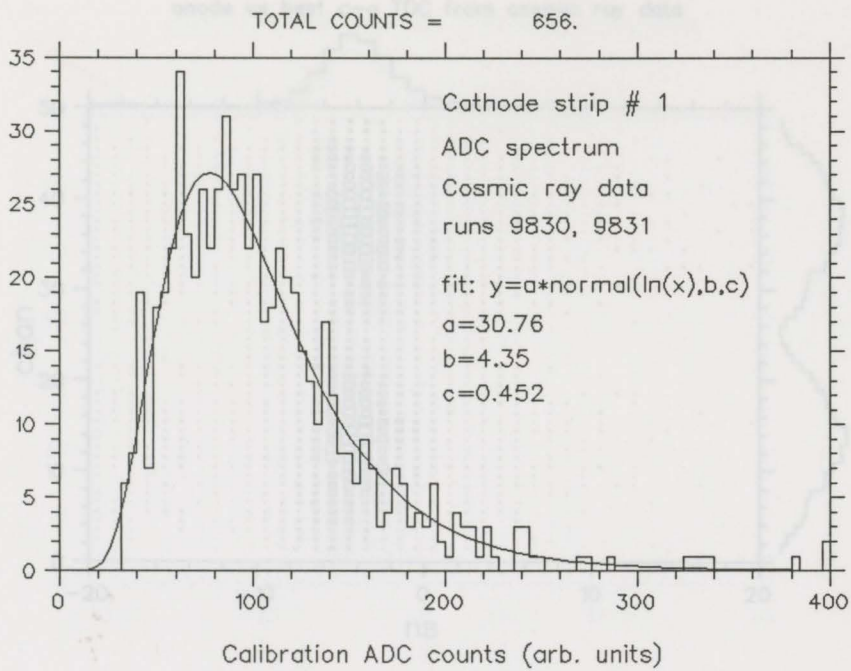


Figure 27: Example cathode strip ADC spectrum.

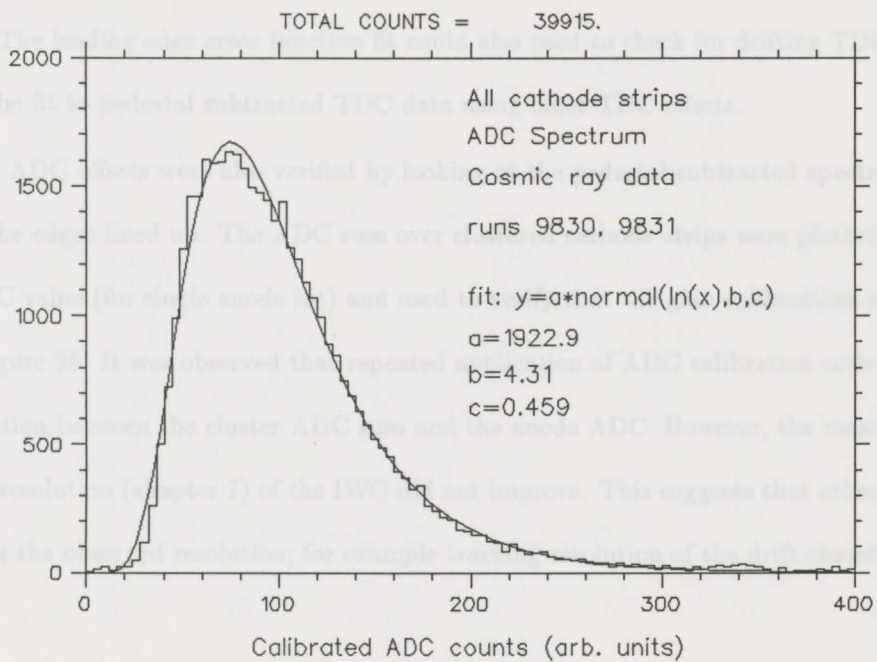


Figure 28: Sum of cathode strip ADC spectra.

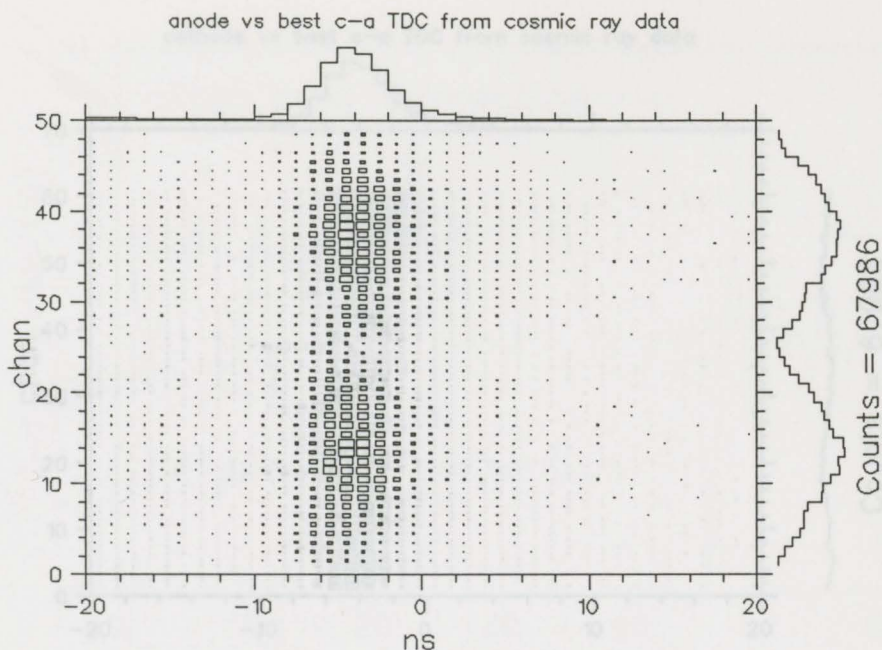


Figure 29: Cathode - anode TDC times for each anode.

observed. The leading edge error function fit could also be used to check for drifting TDC offsets by applying the fit to pedestal subtracted TDC data using older TDC offsets.

The ADC offsets were also verified by looking at the pedestal subtracted spectra and noting how well the edges lined up. The ADC sum over clustered cathode strips were plotted versus anode ADC value (for single anode hit) and used to verify that the gain calibrations were working. Refer to figure 35. It was observed that repeated application of ADC calibration code improved the correlation between the cluster ADC sum and the anode ADC. However, the measured z-position resolution (chapter 7) of the IWC did not improve. This suggests that other factors were dominating the observed resolution; for example tracking resolution of the drift chamber.

Figure 31: Improvement in z-x means for wires.

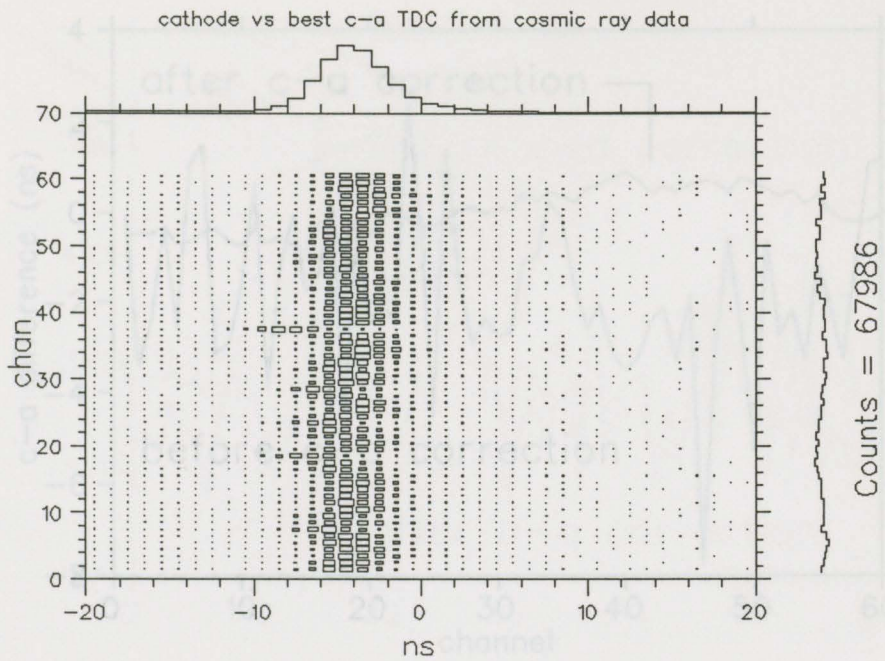


Figure 30: Cathode - anode TDC times for each cathode.

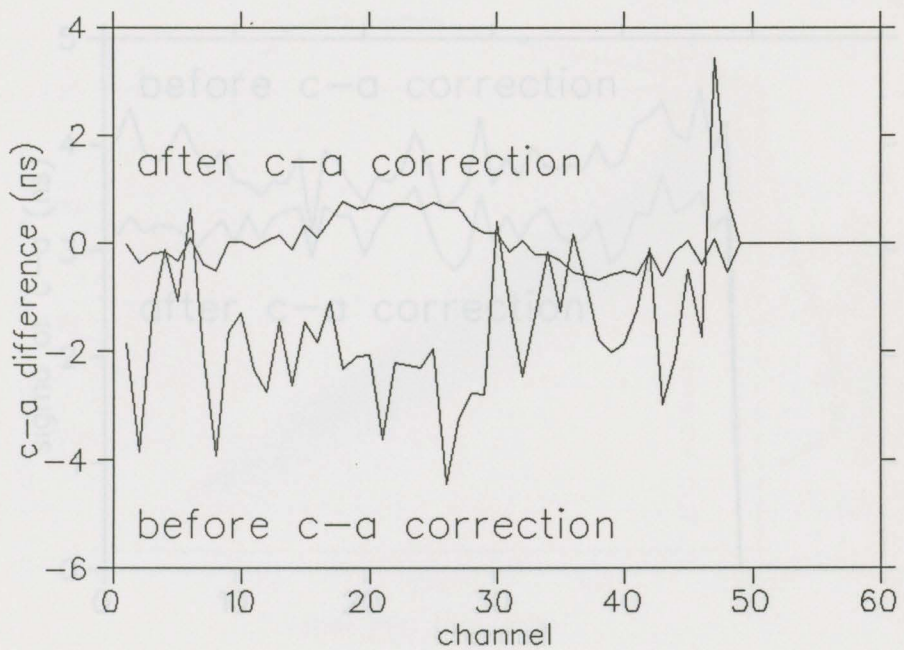


Figure 31: Improvement in c-a means for wires.

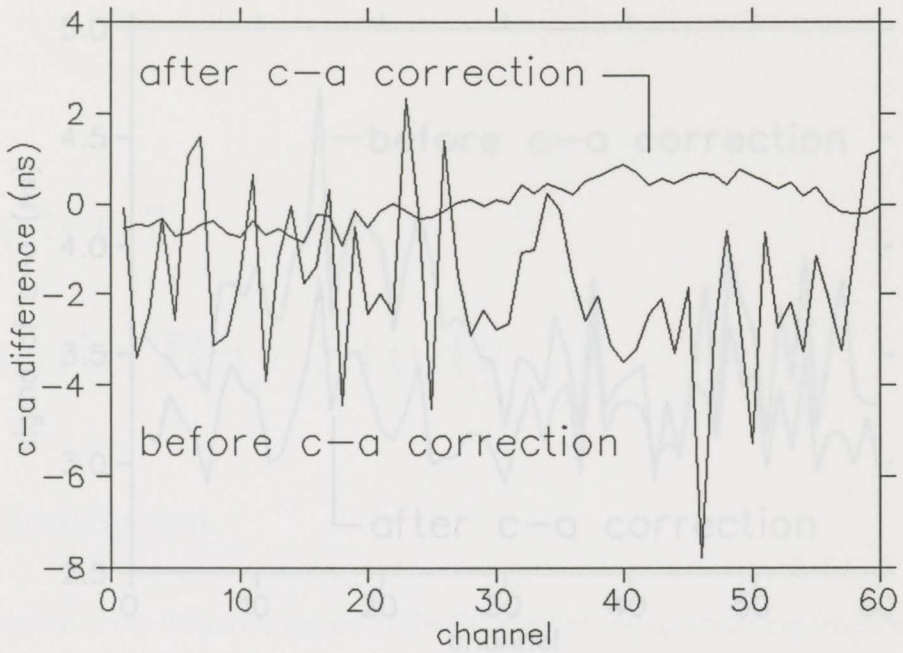


Figure 32: Improvement in c-a means for strips.

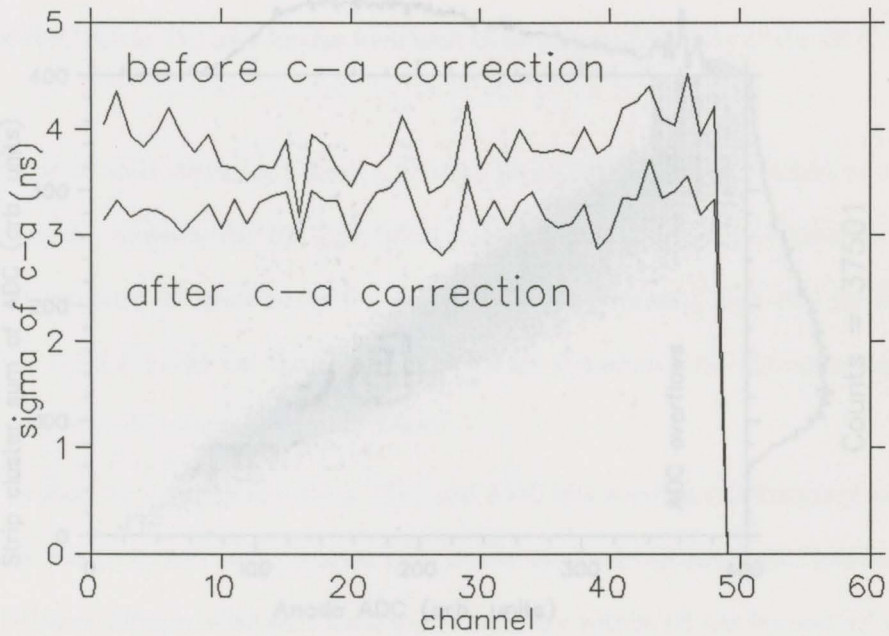


Figure 33: Improvement in c-a sigmas for wires.

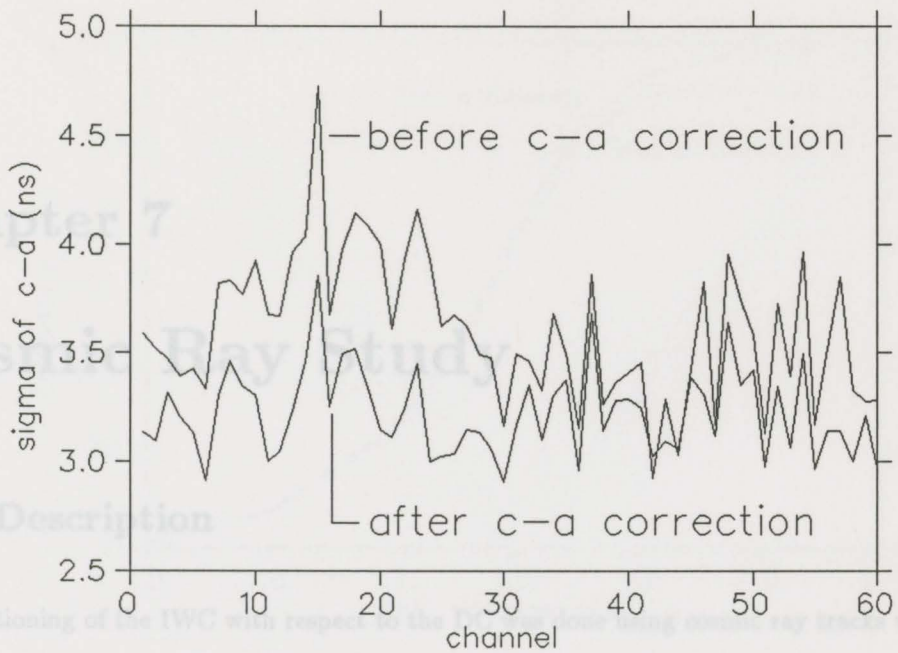


Figure 34: Improvement in c-a sigmas for strips.

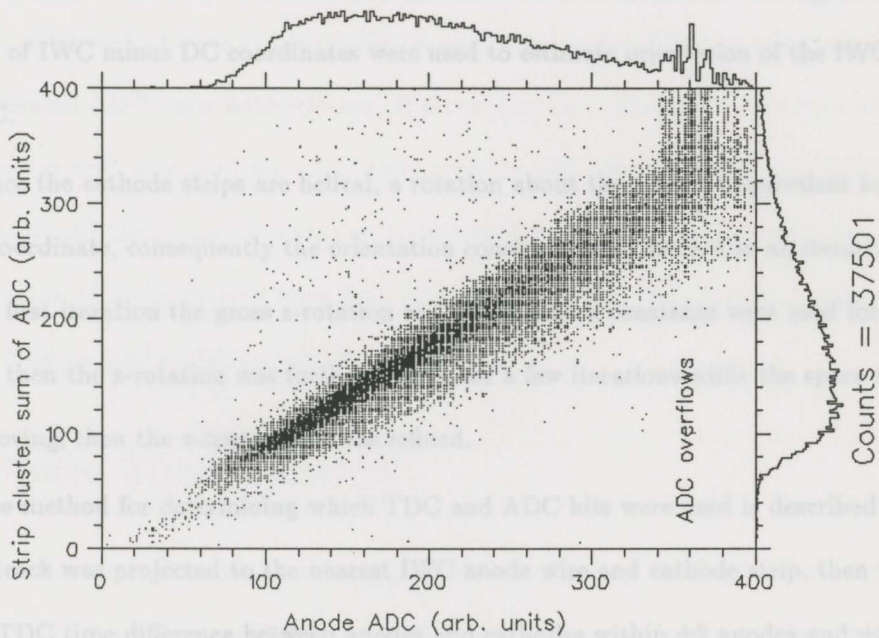


Figure 35: Strip ADC sum vs anode ADC.

Chapter 7

Cosmic Ray Study

7.1 Description

The positioning of the IWC with respect to the DC was done using cosmic ray tracks with the magnetic field off. The tracks found by the DC tracking code were projected into the IWC and the anodes and cathodes near the expected intersection point were searched for valid TDC and ADC information from which the IWC measured intersections were calculated. Histograms of the difference of IWC minus DC coordinates were used to estimate orientation of the IWC with respect to the DC.

Since the cathode strips are helical, a rotation about the z axis is equivalent to a translation in the z -coordinate, consequently the orientation constants were derived in an iterative fashion. After the first iteration the gross z -rotation and z -translation constants were used for the second iteration; then the z -rotation was further refined for a few iterations while the space time relation was improving, then the z -translation was refined.

The method for determining which TDC and ADC hits were used is described as follows. The DC track was projected to the nearest IWC anode wire and cathode strip, then the minimum absolute TDC time difference between anodes and cathodes within ± 2 anodes and ± 6 cathodes was found. The search window was recentered about this best pair, then an ADC weighted z average was done using up to 2 anodes (for cell crossings) and up to 13 strips ($2*6+1$).

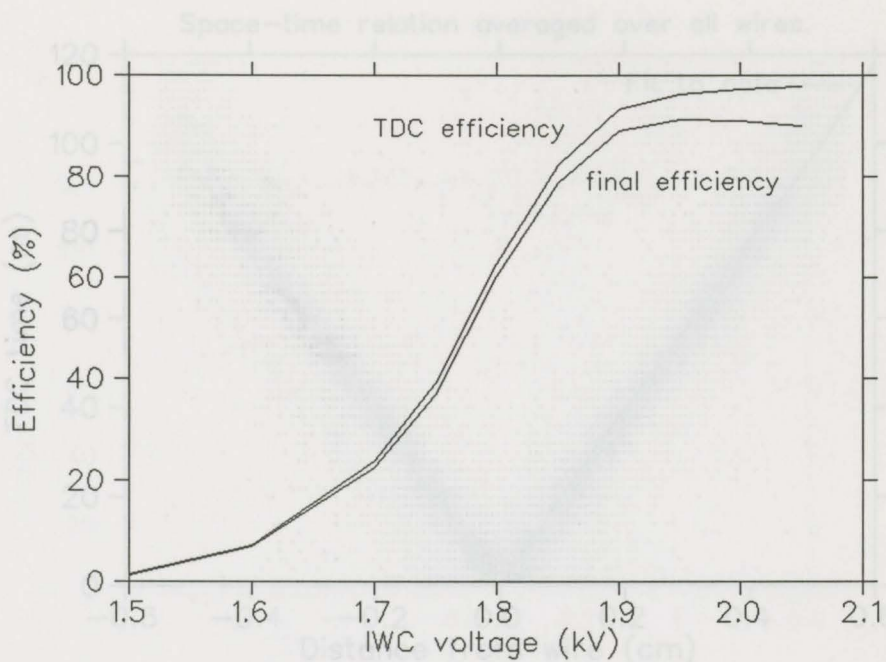


Figure 36: IWC efficiency versus high voltage for $K\mu 2$ data.

The intersections were precalculated (to save time) and ADC data below a noise threshold of 1.0 calibrated ADC units were rejected. If more than two adjacent anodes were hit (within 200 ns, the longest drift time, and the ADC gate) then the IWC data was rejected. The inefficiency of the threshold and anode number cuts can be observed in the difference between the curves in Figure 36; this data was derived from $K\mu 2$ ($K^+ \rightarrow \mu^+ \nu_\mu$) data using the same software with magnetic field on, and a different set of constants.

7.2 Space Time Relation

An approximate space time relation was obtained by calculating the DC track's point of closest approach (POCA) to the anode wire and plotting the pedestal subtracted TDC value versus this distance. As shown in Figure 37, the sign of the distance was defined to be positive if the projected hit position was clockwise of the anode position (clockwise with respect to x-axis looking

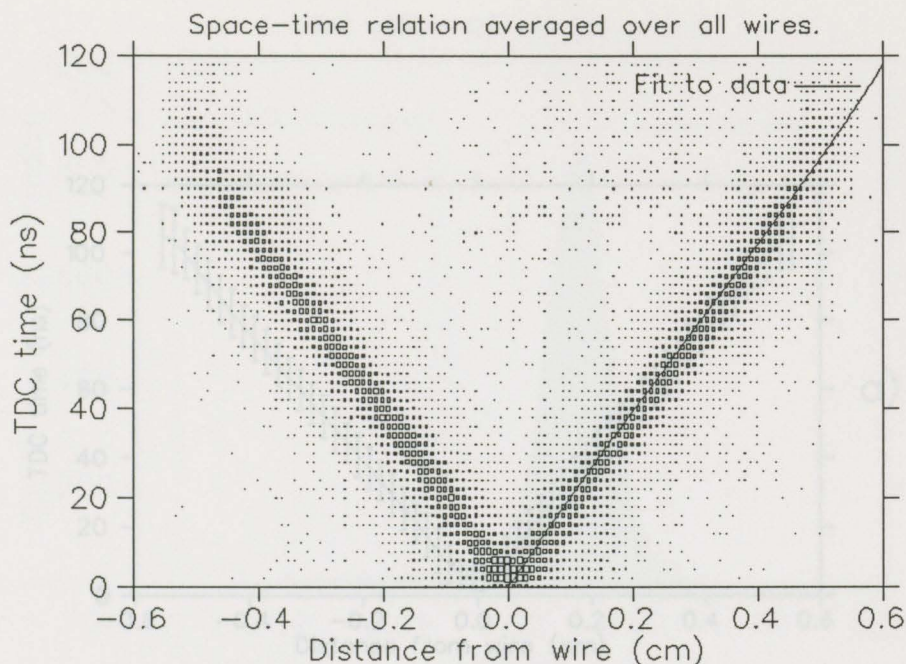


Figure 37: Anode TDC vs POCA.

upstream). The derivative of the space time relations show a relatively constant drift velocity of $50 \mu\text{m}/\text{ns}$ (at 2.0 kV). Refer to Figure 38.

7.3 Rotation

The left-right displacement of the vertex in the space-time plots yield a good estimate of rotation (displacement divided by 8.5 cm equals rotation). The space time relation was used in subsequent iterations to calculate the position of track's primary ionization by assuming circular isochrones and projecting the TDC derived distance in the direction of the expected (DC) hit location. In these subsequent iterations, the angular difference between the IWC (measured) and the DC (expected) hit positions was histogrammed and the mean value was used to further refine the rotation parameter. Figure 39 contains a histogram of the angular difference before any corrections were applied.

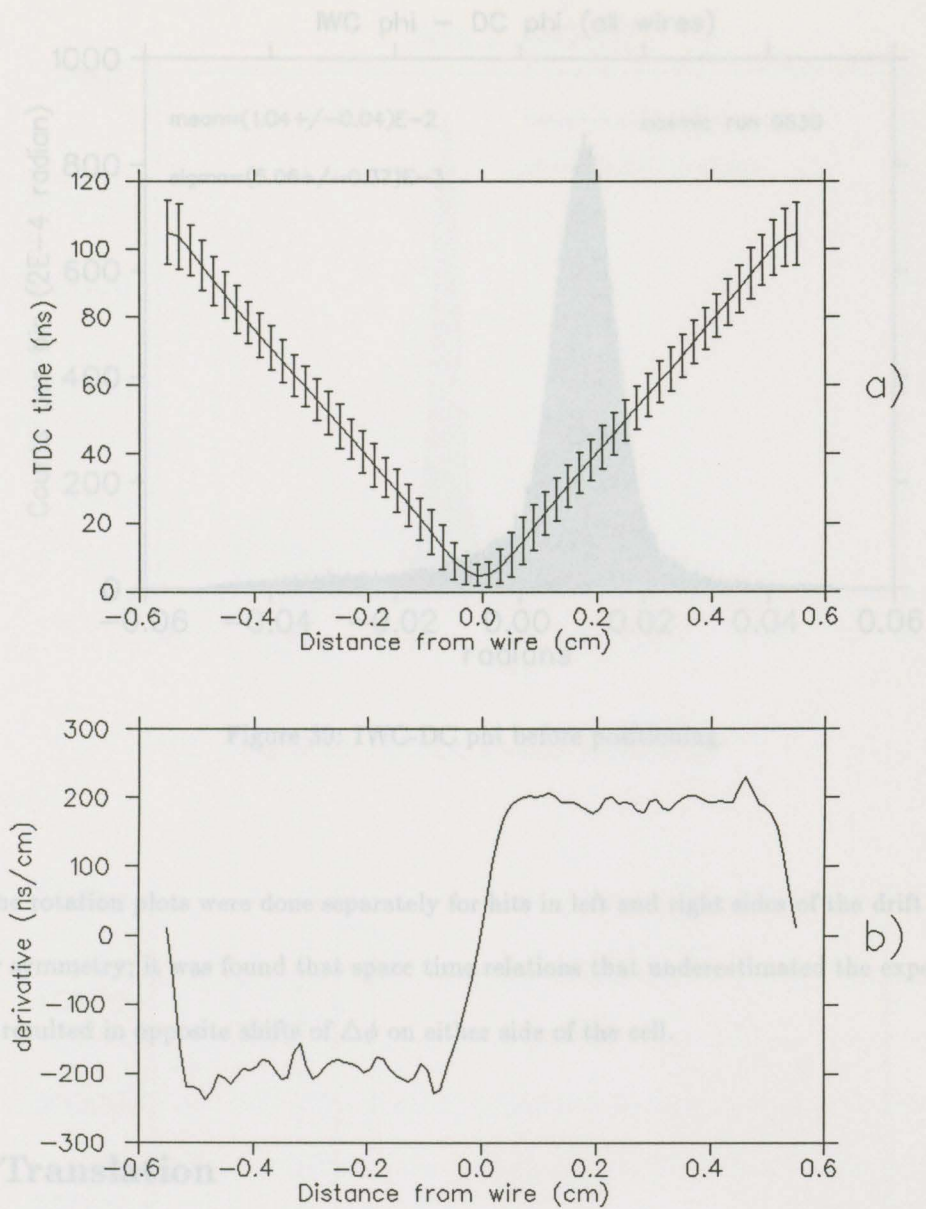


Figure 38: Fit of TDC vs POCA (a) and its derivative (b).

The IWC translation along the x -axis was determined by taking the difference of the projected x position minus the ADC weighted average of strip-wise x -positions. Figure 40 contains a histogram of the translation

The number of strips per cluster per wire is typically five as illustrated in Figure 41. There were usually one or two anodes within the anode window satisfying the ADC threshold cut and within 200 ns of each other as demonstrated in Figure 42.

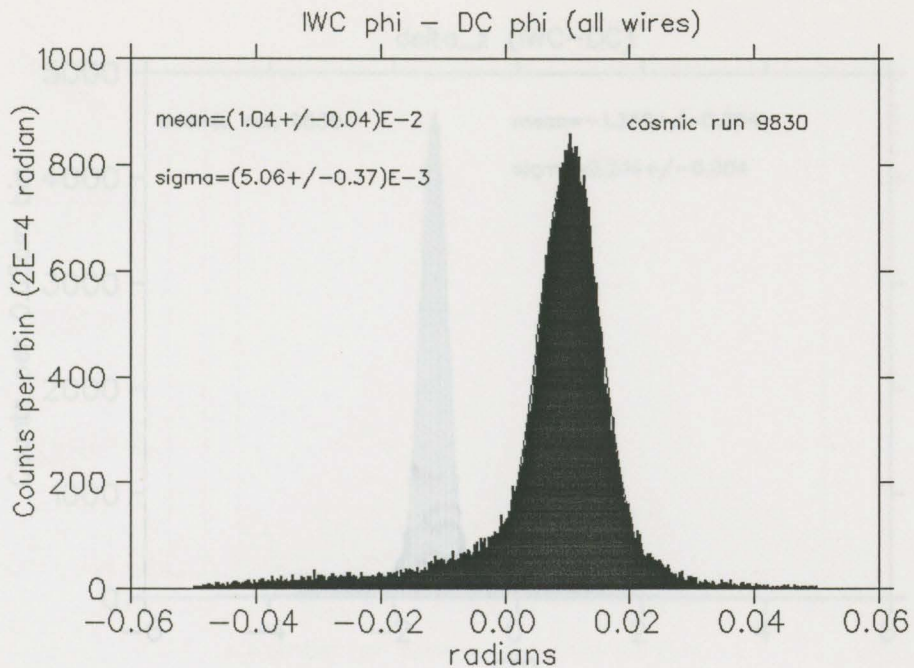


Figure 39: IWC-DC phi before positioning.

The rotation plots were done separately for hits in left and right sides of the drift cell to check for symmetry; it was found that space time relations that underestimated the expected distance resulted in opposite shifts of $\Delta\phi$ on either side of the cell.

7.4 Translation

The IWC translation along the z-axis was determined by taking the difference of the projected z position minus the ADC weighted average of strip-wire z-positions. Figure 40 contains a histogram of the translation difference before any corrections were applied.

The number of strips per cluster per wire is typically five as illustrated in Figure 41. There were usually one or two anodes within the anode window satisfying the ADC threshold cut and within 200 ns of each other as demonstrated in Figure 42.

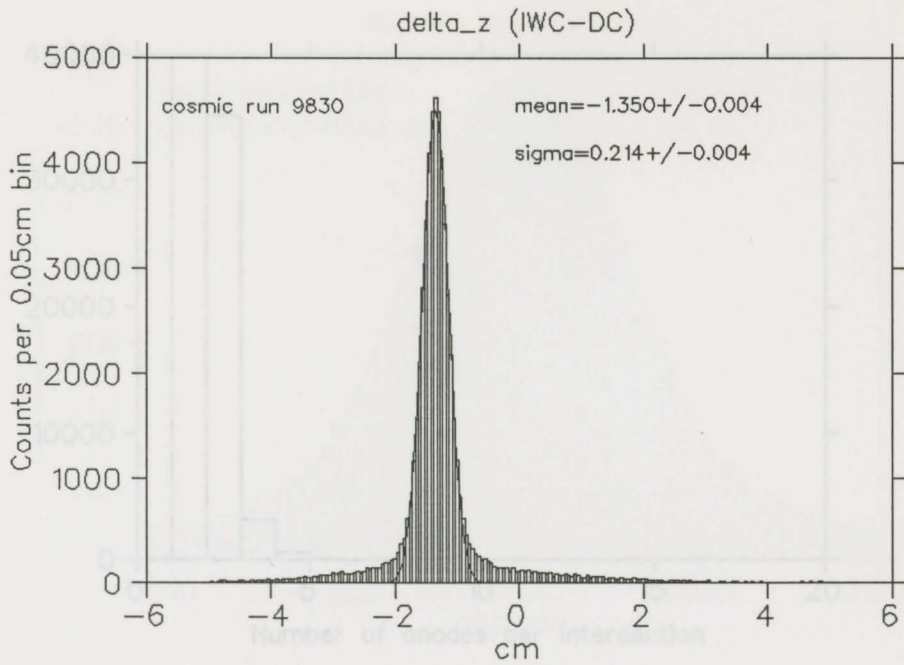


Figure 40: IWC-DC z before positioning.

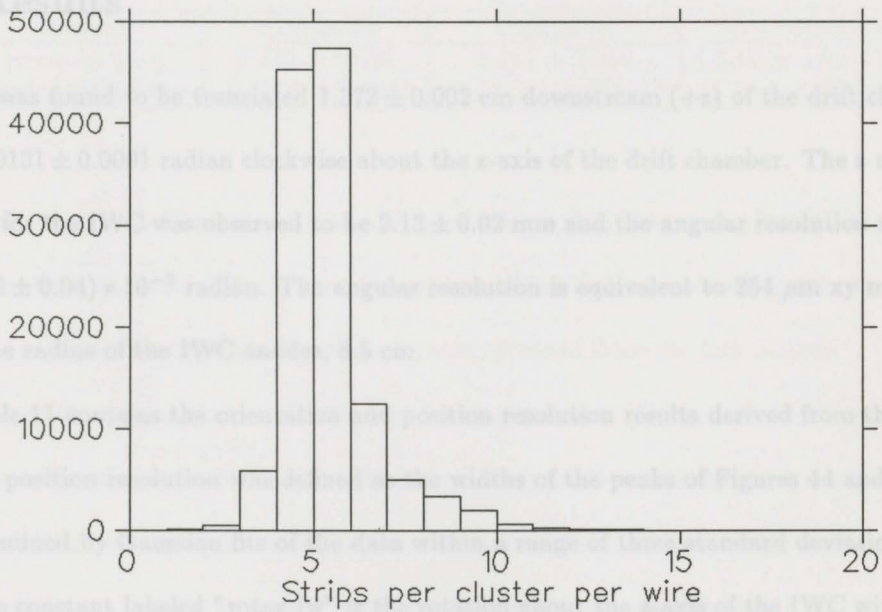


Figure 41: Number of strips per cluster per wire.

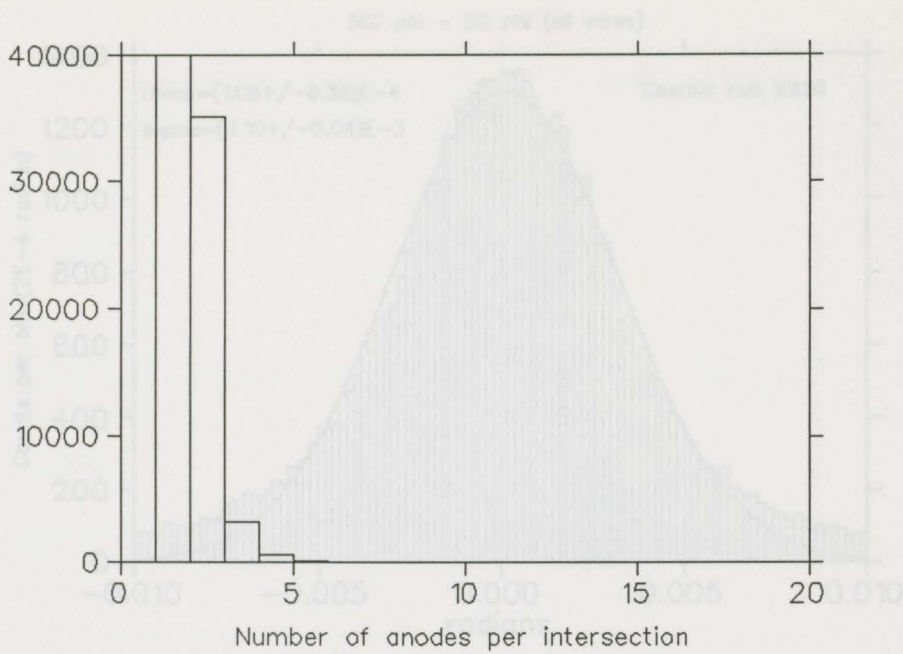


Figure 42: Number of valid anode wires near expected hit.

7.5 Results

The IWC was found to be translated 1.372 ± 0.002 cm downstream (+z) of the drift chamber and rotated 0.0131 ± 0.0001 radian clockwise about the z-axis of the drift chamber. The z measurement resolution for the IWC was observed to be 2.13 ± 0.02 mm and the angular resolution was observed to be $(3.10 \pm 0.04) \times 10^{-3}$ radian. The angular resolution is equivalent to $264 \mu\text{m}$ xy measurement error at the radius of the IWC anodes, 8.5 cm.

Table 11 contains the orientation and position resolution results derived from the cosmic data. The position resolution was defined as the widths of the peaks of Figures 44 and 43 which were determined by Gaussian fits of the data within a range of three standard deviations of the mean. The constant labeled "rotnz_iw" is the rotation about the z-axis of the IWC with respect to the DC. The constant labeled "tranz_iw" is the translation along the z-axis of the IWC with respect to the DC. The column labeled "resolution" is the width of the corresponding histograms

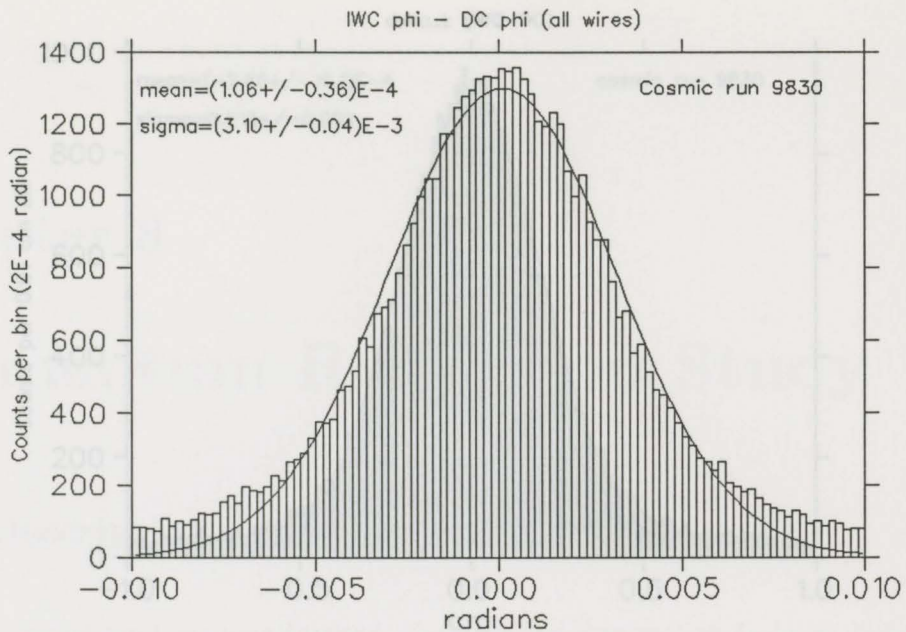


Figure 43: IWC-DC phi after positioning.

Table 11: IWC orientation results from cosmic study.

constant	orientation	resolution	last correction
tranz_iw (cm)	1.372 ± 0.002	0.213 ± 0.002	$(-2.66 \pm 19.1) \cdot 10^{-4}$
rotnz_iw (radian)	-0.0131 ± 0.0001	$(3.10 \pm 0.04) \cdot 10^{-3}$	$(1.16 \pm 0.36) \cdot 10^{-4}$

from the last iteration. The column labeled "last correction" is the mean of the histograms from the last iteration; these corrections would have been added to tranz_iw and rotnz_iw in the next iteration. The errors for orientation constants were obtained from the last column.

Both of the resolutions are slightly larger than expected. The z-resolution is not much better than what would be obtained if only a single strip and wire intersection were used (2.4 mm) and is worse than the expected resolution for an ADC weighted average of five strips (1.07 mm). The xy-resolution is better than what would be obtained if only the identity of the wire and the left-right ambiguity were resolved (1.59 mm), but is higher than the typical drift chamber resolution (150 μm).

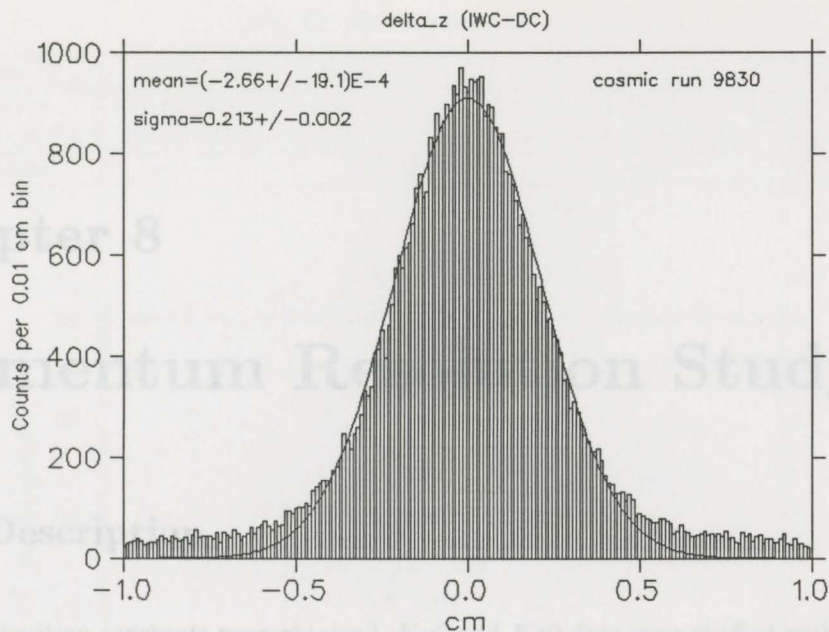


Figure 44: IWC-DC z after positioning.

The following possible resolution contributing factors were rejected: the magnetic field, since the magnet was off; the error due to multiple scattering, since most cosmic ray particles were muons with high momentum (2 GeV/c); the error due to position measurement error of the drift chamber wires. The drift chamber z-resolution of cosmic ray tracks at the IWC was estimated as 0.46 mm and the xy-resolution was estimated as 30 μm . These estimates were obtained by simulating the 150 μm xy position resolution of the drift chamber wires in a simple Monte Carlo study.

Other factors that might have contributed to the slightly higher than expected position resolutions include drift chamber tracking errors due to errors in calibration constants, inaccurate tracking algorithms, and as of yet unidentified software faults. It is possible that the cosmic ray data sample required more stringent cuts; the cuts used were: only one DC reconstructed track per event, and a minimum of two good TDC hits per drift chamber layer.

Table 12: Momentum resolution results

case	$K\mu 2$ mean	$K\mu 2$ sigma	% res	$K\pi 2$ mean	$K\pi 2$ sigma	% res
IWC only	233.06 MeV/c	5.37 MeV/c	2.35	233.69 MeV/c	4.78 MeV/c	2.05
IWC xy and z	233.79 MeV/c	4.66 MeV/c	2.00	234.18 MeV/c	4.25 MeV/c	2.05
Δ sigma	—	13.3 %	—	—	11.1 %	—

Chapter 8

Momentum Resolution Study

8.1 Description

After the position constants were obtained, $K\mu 2$ and $K\pi 2$ data were studied with and without the IWC. For this data the magnetic field was turned on so different space-time relations were required because of twisted drift lines and squashed isochrones. In addition, a different set of TDC offsets were needed because of differences between normal and cosmic ray triggers, one of which is a 14 ns time difference due to the trigger hardware.

An iterative method was used to obtain a reasonable space-time relation for the $K\mu 2$ data.

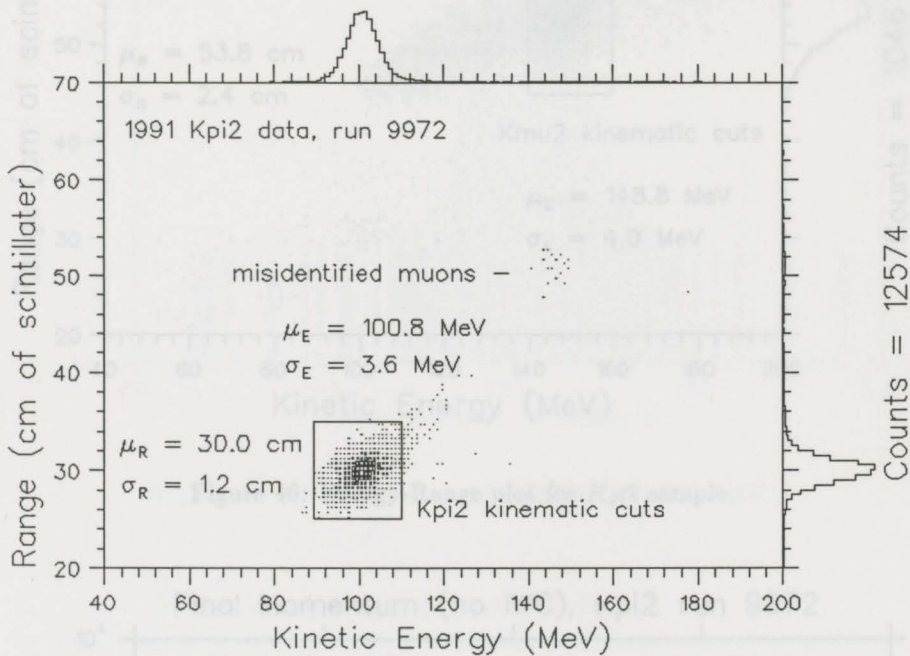
The method uses some starting space-time relation such as the one obtained by TDC versus POCA plots, then uses residuals as function of TDC time to improve the relation.

Figures 45 and 46 contain range versus energy distributions for the $K\pi 2$ and $K\mu 2$ data used. Data for which the IWC tracking failed was rejected so that a fair comparison of results with and without IWC could be made. Both data sets had a delayed coincidence cut of two nanoseconds applied to pion (muon) minus kaon time as found in the target; events with a time difference less than two nanoseconds were rejected. For the $K\pi 2$ data the KOFIA transient digitizer (TD) fitting routine, FITPI, was applied to obtain a clean sample of pions.

The $K\mu 2$ momentum resolution was measured as 2.35% without the IWC and 2.00% with the IWC. The $K\pi 2$ momentum resolution was measured as 2.35% without the IWC and 2.08%

Table 12: Momentum resolution results.

case	$K\mu 2$ mean	$K\mu 2$ sigma	% res	$K\pi 2$ mean	$K\pi 2$ sigma	% res
DC only	233.05 MeV/c	5.47 MeV/c	2.35	203.60 MeV/c	4.78 MeV/c	2.35
IWC xy and z	233.79 MeV/c	4.68 MeV/c	2.00	204.18 MeV/c	4.25 MeV/c	2.08
Δ sigma	—	14.4 %	—	—	11.1 %	—

Figure 45: Energy-Range plot for $K\pi 2$ sample.

with the IWC. Table 12 contains the momentum resolution results and Figures 47,48,49, and 50 illustrate the final momentum spectra. The data was fit with Gaussian functions using the full range of data.

8.2 Comparison with Monte Carlo Results

The momentum resolution for $K\pi 2$ data is worse than the Monte Carlo predictions as can be observed by comparing Figures 9 and 10 with Figures 47 and 48. However, the relative improvement in the momentum resolution for $K\pi 2$ data, 11%, agrees with the Monte Carlo

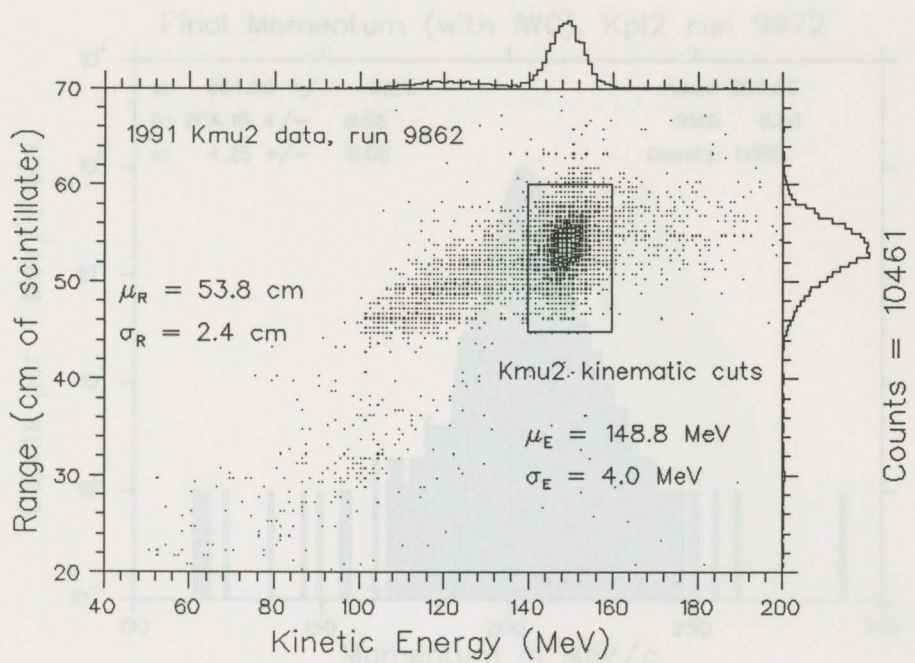


Figure 46: Energy-Range plot for $K\mu 2$ sample.

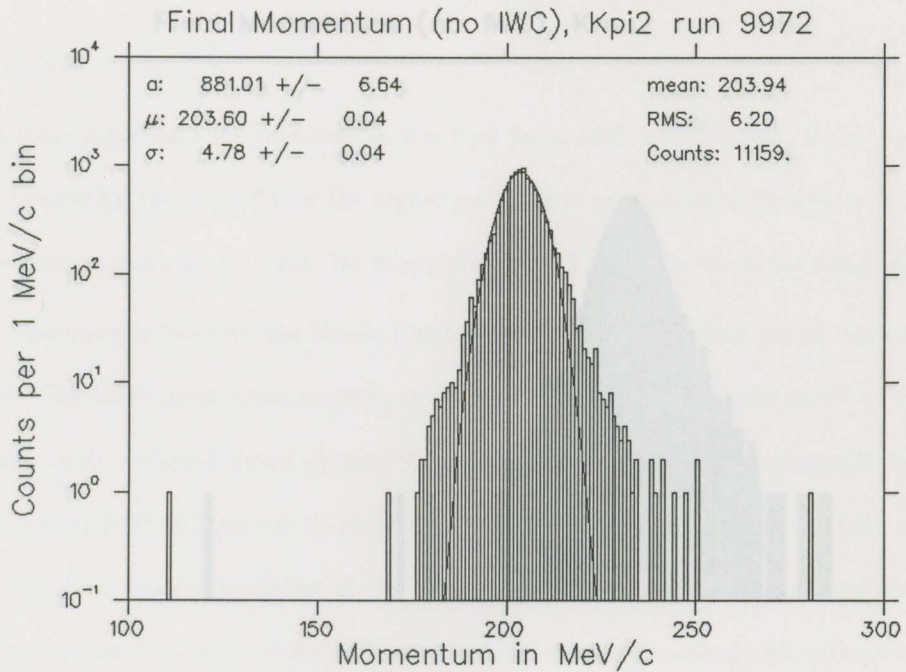
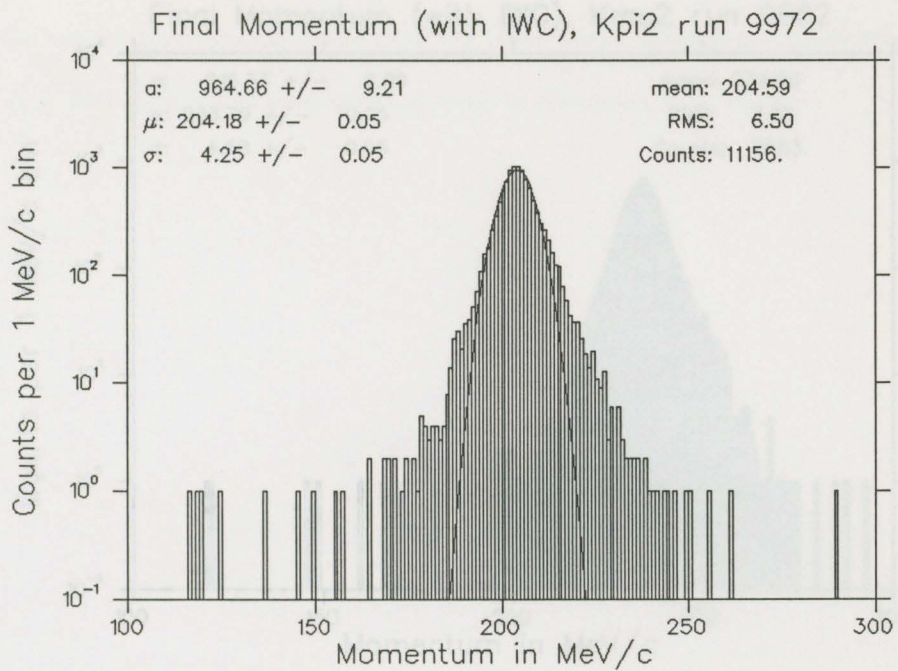
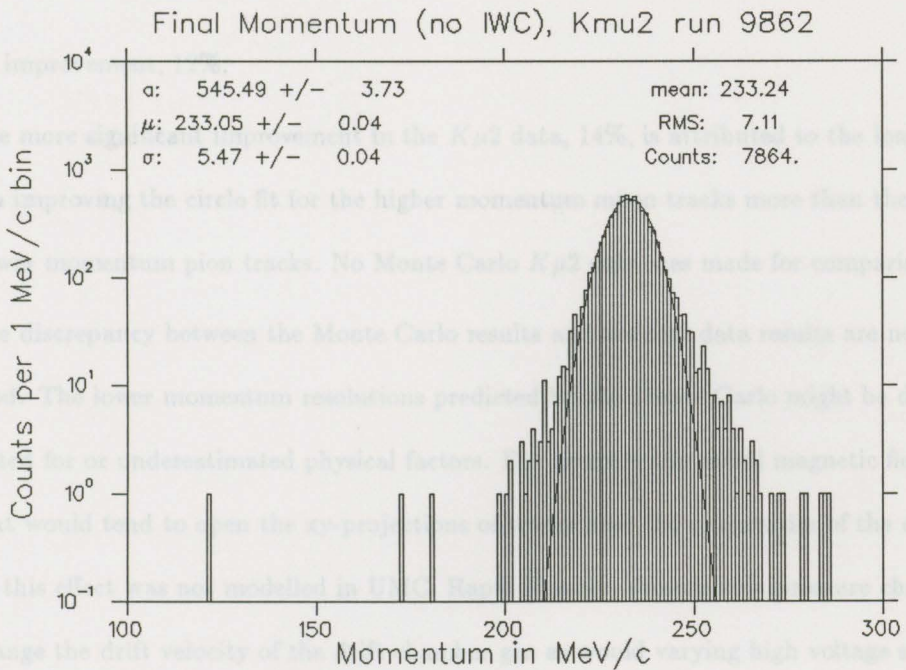
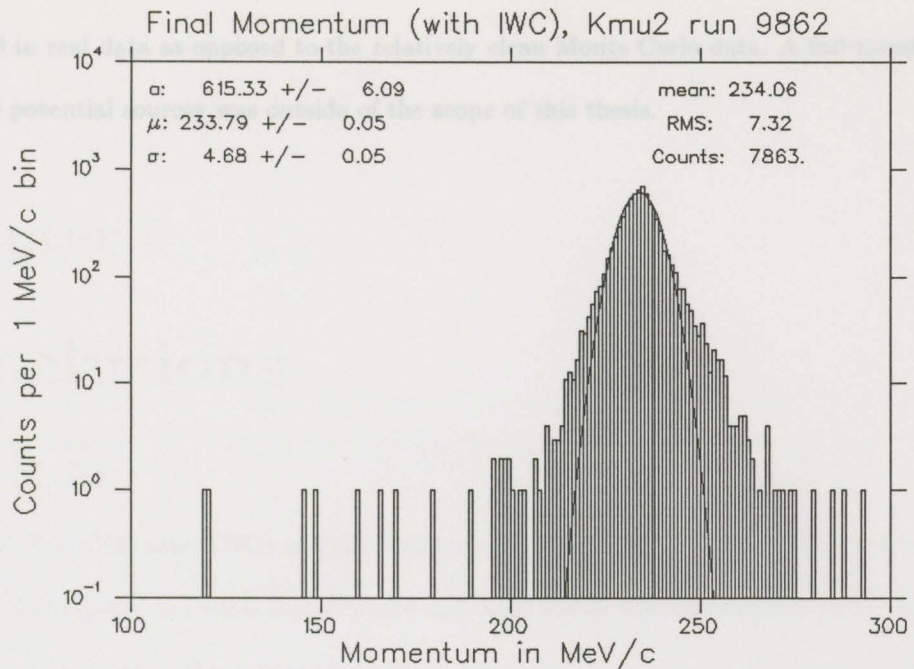


Figure 47: $K\pi 2$ final momentum spectrum without IWC.

Figure 48: $K\pi^2$ final momentum spectrum with IWC.Figure 49: $K\mu^2$ final momentum spectrum without IWC.

Figure 50: $K\mu 2$ final momentum spectrum with IWC.

predicted improvement, 12%.

The more significant improvement in the $K\mu 2$ data, 14%, is attributed to the longer arc-length improving the circle fit for the higher momentum muon tracks more than the circle fit for the lower momentum pion tracks. No Monte Carlo $K\mu 2$ data was made for comparison.

The discrepancy between the Monte Carlo results and the real data results are not well understood. The lower momentum resolutions predicted by the Monte Carlo might be due to some unaccounted for or underestimated physical factors. For example the radial magnetic field component would tend to open the xy-projections of tracks near the extremities of the drift chamber; this effect was not modelled in UMC. Rapid (hourly) atmospheric pressure changes would change the drift velocity of the drift chamber gas as would varying high voltage supplies. Variations in the main magnet current would also degrade the momentum resolution. It may be that the drift chamber tracking code is less effective when dealing with the larger number of TDC

hits found in real data as opposed to the relatively clean Monte Carlo data. A full investigation of the above potential sources was outside of the scope of this thesis.

Chapter 9

Conclusions

The Inner Wire Chamber (IWC) is a thin cylindrical proportional drift chamber which uses the coincidence of signals on helical copper strips and axial anode wires to measure xyz coordinates of charged particle tracks. The copper strips were chemically etched from a thin vacuum deposited layer of copper on a thin polyimide film. This design was favoured over other possible designs because of its low mass. The purpose of the chamber is to improve the charged particle tracking and thus improve the momentum resolution of the E787 detector.

The position resolution of the IWC was measured as 9.13 mm in the z coordinate and 0.264 mm in the x and y coordinates. These are the results of a study using cosmic-ray data and the present E787 drift chamber.

It has been demonstrated that the IWC improves the momentum resolution of the E787 detector. The momentum resolution for 1991 $K\gamma 2$ data without the IWC is 2.35%, whereas the resolution with the IWC is 2.03%. The momentum resolution for 1991 $K\mu 2$ data without the IWC is 2.33%, whereas the resolution with the IWC is 2.00%.

It has also been demonstrated that the methods and materials used to construct this kind of chamber are practical. The experience gained during construction of the IWC will prove beneficial during the construction of the next E787 drift chamber, the UTC.

Chapter 9

Conclusions

The Inner Wire Chamber (IWC) is a thin cylindrical proportional drift chamber which uses the coincidence of signals on helical copper strips and axial anode wires to measure xyz coordinates of charged particle tracks. The copper strips were chemically etched from a thin vacuum deposited layer of copper on a thin polyermide film. This design was favoured over other possible designs because of its low mass. The purpose of the chamber is to improve the charged particle tracking and thus improve the momentum resolution of the E787 detector.

The position resolution of the IWC was measured as 2.13 mm in the z coordinate and 0.264 mm in the x and y coordinates. These are the results of a study using cosmic ray data and the present E787 drift chamber.

It has been demonstrated that the IWC improves the momentum resolution of the E787 detector. The momentum resolution for 1991 $K\pi^2$ data without the IWC is 2.35%, whereas the resolution with the IWC is 2.08%. The momentum resolution for 1991 $K\mu^2$ data without the IWC is 2.35%, whereas the resolution with the IWC is 2.00%.

It has also been demonstrated that the methods and materials used to construct this kind of chamber are practical. The experience gained during construction of the IWC will prove beneficial during the construction of the next E787 drift chamber, the UTC.

Bibliography

- [1] C. Q. Geng and John N. Ng, *Constraints on t -quark mass and quark mixings from $K_L \rightarrow \mu\bar{\mu}$, and relations to other rare decays*, Physical Review D, Volume 41, Number 7, pp. 2351-2354, April 1, 1990.
- [2] Laurence S. Littenberg, *The relation between $B(K^+ \rightarrow \pi^+\nu\bar{\nu})$ and V_{td}* , E787 technical note #179, Brookhaven National Laboratory, Upton, New York, USA, October 18, 1990
- [3] John Haggarty, *Determination of Standard Model Parameters from $K^+ \rightarrow \pi^+\nu\bar{\nu}$* , E787 technical note #196, Brookhaven National Laboratory, Upton, New York, USA, November 6, 1990
- [4] S. L. Wu, *New Results from LEP*, Particles and Fields Conference, Plenary Session II, University of British Columbia, August, 1991.
- [5] William J. Marciano, *The Standard Model and Beyond*, BNL document number 42855, May, 1989.
- [6] John A. Macdonald, *A Detector to Search for $K^+ \rightarrow \pi^+\nu\bar{\nu}$* , NIM paper to be published, TRIUMF, draft #1, Nov. 19, 1990
- [7] Douglas Bryman, *Rare Kaon Decay Experiments*, International Journal of Modern Physics, Vol. 4, Page 79, 1989
- [8] Douglas Bryman, *Rare Kaon Decays*, TRIUMF Pre-Print-88-48, June, 1988
- [9] J. V. Cresswell et al., *A Cylindrical Drift Chamber for the Measurement of $K^+ \rightarrow \pi^+\nu\bar{\nu}$* , IEEE Transactions on Nuclear Science, Vol. 35, No. 1, pp. 460-463, February, 1988
- [10] E.W. Blackmore et al, *Ultra Thin drift Chamber for E787*, E787 technical note #182, TRIUMF, British Columbia, Canada, February 12, 1991
- [11] Y. Kuno, *Monte Carlo Study of Ultra Thin drift Chamber (UTC)*, E787 technical note #200, TRIUMF, British Columbia, Canada, January 28, 1991
- [12] Robert A. McPherson et al., *The Foil Chamber Prototype*, E787 technical note #212, Princeton, New Jersey, USA, August 7, 1991

- [13] Particle Data Group, *Review of Particle Properties*, Physics Letters, Vol. 239, page III.23, April, 1990
- [14] Y. Kuno, A. Turcot, V. Kujala *A Monte Carlo Study of the Proposed IWC and Straw Tubes*, E787 technical note #194, TRIUMF, British Columbia, Canada, September, 1990
- [15] R. Walter et al., *The EGS4 Code System*, SLC publication SLAC-265 UC-32
- [16] Gordon Greeniaus, *LOSSPROG*, Software that estimates multiple scattering and energy loss in various media, TRIUMF, June, 1990
- [17] Rob Veenhoff, *GARFIELD, a drift chamber simulation program v2.02*, CERN, 1990
- [18] F. Sauli, *Principles of Operation of Multiwire Drift and Proportional Chambers*, CERN report 77-09, May 03, 1977
- [19] *Broadband Amplifier Applications*, Plessey Semiconductors, September, 1984
- [20] *Lecroy 1990 Research Instrumentation Catalog*, September, 1989
- [4] John R. Bass, *The Stanford Linear Collider*, Scientific American, Inc., October, 1989
- [5] Stephen Myers and Emilio Picasso, *The LEP Collider*, Scientific American, Inc., July, 1980
- [6] Gary J. Feldman and Jack Steinberger, *The Number of Families of Neutrinos*, Scientific American, Inc., February, 1981
- [7] Horst Brinker et al., *Tracking and Imaging Elementary Particles*, Scientific American, Inc., August, 1991
- [8] Leo Stodolsky, *Neutrino and Dark Matter Detection at Low Temperatures*, Physics Today, page 24, August, 1991
- [9] Bernard Sadoulet and James W. Cronin, *Particle Astrophysics*, Physics Today, page 53, April, 1991

Suggested Reading

- [1] Robert N. Cahn and Gerson Goldhaber, *The Experimental Foundations of Particle Physics*, Cambridge University Press, 1989
- [2] David Griffiths, *Introduction to Elementary Particles*, Harper & Row Publishers, Inc., 1987
- [3] Donald H. Perkins, *Introduction to High Energy Physics*, third edition, Addison-Wesley Publishing Company, Inc., 1987
- [4] John R. Rees, *The Stanford Linear Collider*, Scientific American, Inc., October, 1989
- [5] Stephen Myers and Emilio Picasso, *The LEP Collider*, Scientific American, Inc., July, 1990
- [6] Gary J. Feldman and Jack Steinberger, *The Number of Families of Matter*, Scientific American, Inc., February, 1991
- [7] Horst Breuer et al., *Tracking and Imaging Elementary Particles*, Scientific American, Inc., August, 1991
- [8] Leo Stodolsky, *Neutrino and Dark Matter Detection at Low Temperature*, Physics Today, page 24, August, 1991
- [9] Bernard Sadoulet and James W. Cronin, *Particle Astrophysics*, Physics Today, page 53, April, 1991

eV, a convenient unit for measuring elementary particle energies. One *eV* equals (approximately) 1.6×10^{-19} joules. These units are used with standard metric prefixes. Particle energies in nuclear physics are typically hundreds of *MeV*. Particle energies in high energy particle physics are typically tens of *GeV*.

eV/c, a convenient unit for measuring elementary particle momenta. One *eV/c* equals (approximately) 3.3×10^{-28} kilogram-meter-per-second. These units are used with standard metric prefixes. For example, *MeV/c* and *GeV/c* are typical momenta for medium and high energy particles.

eV/c², a convenient unit for measuring elementary particle masses. One *eV/c²* equals (approximately) 1.8×10^{-36} kilograms. These units are used with standard metric prefixes. For example the rest mass of the electron is $0.511 \text{ MeV}/c^2$.

Glossary

ADC, Analog to Digital Converter. An electronic device used to measure voltages and present the results in a form readable by computers.

AGS, Alternating Gradient Synchrotron. A charged particle accelerator which uses reversing electromagnetic fields.

Ar, the element argon

BeO, the compound Berillium Oxide.

BNL, Brookhaven National Laboratories. A collection of nuclear and particle physics research facilities on Long Island, New York.

DC, the main Drift Chamber used for tracking charged particles in experiment E787.

E787, Brookhaven National Laboratories Experiment number 787. An experiment designed to look for the rare kaon decay, $K^+ \rightarrow \pi^+ \nu \bar{\nu}$.

EGS, Electron Gamma Shower. Software used to simulate the passage of electrons and photons through matter. Energetic electrons will interact with matter and create showers of many lower energy electrons and photons.

Et, the organic molecule ethane.

eV, a convenient unit for measuring elementary particle energies. One eV equals (approximately) $1.6 * 10^{-19}$ joules. These units are used with standard metric prefixes. Particle energies in nuclear physics are typically hundreds of MeV. Particle energies in high energy particle physics are typically tens of GeV.

eV/c, a convenient unit for measuring elementary particle momenta. One eV/c equals (approximately) $5.3 * 10^{-28}$ kilogram-meter-per-second. These units are used with standard metric prefixes. For example, MeV/c and GeV/c are typical momenta for medium and high energy particles.

eV/c², a convenient unit for measuring elementary particle masses. One eV/c² equals (approximately) $1.8 * 10^{-36}$ kilograms. These units are used with standard metric prefixes. For example the rest mass of the electron is $0.511 MeV/c^2$.

Fe^{55} , iron radio-isotope with atomic number 55.

IWC, Inner Wire Chamber. A thin cylindrical drift chamber used for tracking charged particles.

$K\mu 2$, one of the more common decay modes of the kaon, $K^+ \rightarrow \mu^+ \nu_\mu$, with decay fraction 63.5%.

$K\pi 2$, one of the more common decay modes of the kaon, $K^+ \rightarrow \pi^+ \pi^0$, with decay fraction 21.2%.

KOFIA, Kaon OFFline Interactive Analysis. Software used to analyze the data acquired by the E787 detector.

Mhz, one million cycles per second.

POCA, Point Of Closest Approach. The point along some trajectory which is closest to some other specified point.

resolution, the spread of a measurement of some parameter. Typically used to characterize the accuracy of some measurement device.

RMS, Root Mean Square. A number representing the spread of numerical data.

RSPC, Range Stack Proportional Chambers. Gas filled wire chambers operated in proportional gain mode and which are imbedded in the range stack of the E787 detector. They provide additional information for charged particle tracking.

SLAC, Stanford Linear Accelerator Center. An electron/positron accelerator and collider at Stanford University.

TDC, Time to Digital Converter. An electronic device used to measure time intervals and present the results in a form readable by computers.

UMC, Universal Monte Carlo. Software used to simulate particles moving through the E787 detector.

UTC, Ultra Thin Chamber. A cylindrical drift chamber which will replace the present E787 drift chamber in 1992.

PARTIAL COPYRIGHT LICENSE

VITA

I hereby grant the right to lend my thesis to users of the University of Victoria Library, and to make single copies only for such users or in response to a request from the Library of any other university or library on its behalf or for other users. I do not intend to make an extensive use of the thesis for other purposes. I do not intend to use or to authorize the University of Victoria to use or to authorize copying or publication of this thesis for financial gain and not be allowed without my written permission.

Surname: Kujala Given Names: Vincent Anthony
Place of Birth: Edmonton, Alberta, Canada Date of Birth: 12 July 1966

Educational Institutions Attended:

Title of Thesis: An Inner Wave Character for the Neutron
University of Victoria Fall 1984 to Spring 1992

Author: V. Kujala
Signature: V. Kujala
Degrees Awarded:

B.Sc. University of Victoria Spring 1989

V. Kujala

(Name in Block Letters)

Honours and Awards:

NSERC Undergraduate Research Award, May 1989.
The MacDonnell Graduate Award in Physics, October, 1989.

January 1992
(Date)

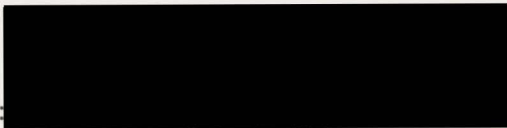
PARTIAL COPYRIGHT LICENSE

I hereby grant the right to lend my thesis to users of the University of Victoria Library, and to make single copies only for such users or in response to a request from the Library of any other university, or similar institution, on its behalf or for one of its users. I further agree that permission for extensive copying of this thesis for scholarly purposes may be granted by me or a member of the University designated by me. It is understood that copying or publication of this thesis for financial gain shall not be allowed without my written permission.

Title of Thesis:

An Inner Wire Chamber for the Measurement of $K^+ \rightarrow \pi^+ \nu \bar{\nu}$

Author:


Signature

V. Kujala

(Name in Block Letters)

Jan 28, 1992
(Date)